The Design and Development of a Scanning Tunneling Microscope and its use for Studying Oxygen Adsorption on Vicinal Copper Surfaces.

Grongar Wynne Woodliffe Lloyd

A thesis submitted for admission to the degree of

Doctor of Philosophy.

Department of Physics

University of Warwick

26th November 1992

VARIABLE PRINT QUALITY

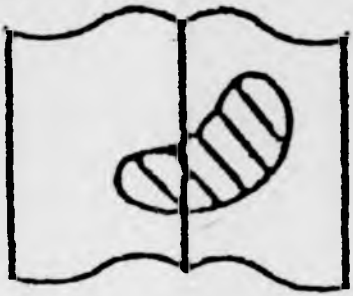

Abstract

A scanning tunneling microscope has been designed and built in the Department of Physics at the University of Warwick which is capable of atomic resolution on metals.

A number of problems associated with the design and manufacture of a Scanning Tunneling Microscope (STM) had to be overcome. The design of an ultra high vaccum chamber and its associated power, gas and water supplies. The removal of vibrations from the vacuum system. The coarse and fine tip approach that enabled the tunneling regime to be entered without tip crash. The design and construction of a novel sample transfer mechanism that enabled electrical connections to be engaged and disengaged automatically when placing the sample into the STM.

A program of testing, development and calibration, firstly in air and then under vacuum, proved the atomic resolution of the instrument.

Oxygen induced faceting of vicinal copper surfaces was imaged with atomic resolution. A new model for the reconstruction of the Cu(410) terraces is proposed.

Contents.

Acknowledgements

I should like to thank the following people for their help and support during the long and difficult period of research and thesis production.

D P Woodruff, my supervisor for invaluable support and advice.

I John for his skills in manufacturing and constructing the STM head and vacuum chamber.

R I Johnston for his mechanical skills in developing and maintaining the system.

I would also like to acknowledge the help and support, both financial and moral, of my family and Rebecca French. Ann and John French for their assistance in the typing of this thesis and Emily Devlin for her assistance with the bibliography, diagrams and printing. Chris McConville for his words of advice and encouragement. Not forgetting SERC for the financial backing of the project.

Declaration

I declare that this thesis contains an account of my research carried out in the Department of Physics at the University of Warwick between October 1987 and October 1992 under the supervision of Professor D P Woodruff. The research described herein has not been submitted either partly or totally at this academic institution or any other for admission to a higher degree. Some parts are currently being published

G W Lloyd and D P Woodruff, Do Oxgen-induced Cu(410) Facets Reconstruct? Surf Sci, In Print.

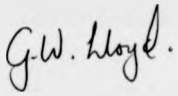

G. W. Lloyd.

Acronyms

AES	Auger electron spectroscopy.
ARUPS	Angle resolved UPS.
DVSTM	Dynamic-visualisation STM.
FIM	Field ion microscopy.
HREELS	High resolution electron energy loss spectroscopy.
IPE	Inverse photoemission.
LDOS	Local density of states.
LEED	Low energy electron diffraction.
SEXAFS	Surface extended x-ray absorption fine structure.
STM	Scanning tunneling microscopy.
STS	Scanning tunneling spectroscopy.
UHV	Ultra high vacuum.
UPS	Ultraviolet photoelectron spectroscopy.
XRD	X-ray diffraction.

Chapter 1

Introduction.

Contents

1.1 The relevance of surface science.

A cursory examination of the term 'surface science' might lead one to assume that it has no great relevance to, or bearing on, the real world. However, on closer inspection of our surroundings it becomes apparent that the majority of interactions, be they chemical or physical, between bodies occur at points at which they meet, i.e. their surfaces. The dissolving of solids in liquids, combustion of materials in air and the photosynthesis of plants are but a few of the vast number of reactions that rely either entirely, or in part, on the direct impinging of one material onto the surface of another.

As the result of many years of experience in the chemical industry man has learned to modify some of these reactions for his own benefit, not the least of

which in importance has been the development of catalysts. In such a vast industry an improvement of a few percent in the productivity of a reaction could result in great savings in time, energy and money. If a clearer understanding of the role of catalyst's surface structure and electronic properties in a reaction could be obtained then the possibility of designing cheaper custom built catalysts for specific reactions arises.

A second interest of surface scientists and a major drain on world resources is the degradation of materials by either attack at their surfaces or the migration of defects to form cracks. The rusting of cars, corrosion of chemical pipelines and the cracking of aluminium based alloy components in aircraft, are a few examples where knowledge gained from surface science of the process of oxidation, chemical attack and degradation could be usefully applied.

A third topic of interest is that of passivation of otherwise reactive materials by the application, or natural occurrence, of a non-reactive coating. Painting car bodywork prevents oxidation of the steel, whereas the oxide of aluminium provides protection of the bulk material from further attack.

At present perhaps the most direct application of surface science techniques occurs in the semiconductor industry which is making great advances in the miniaturisation of electronic components and the production of novel devices for both computing and electronic industries. Multi-layered semiconductor devices on single crystal bases are reducing in thickness to such an extent that the properties of the interface must be taken into account.

The vast majority of the above mentioned surface related reactions, however,

take place in non-trivial conditions on poly-crystalline materials, and bear little resemblance to the current practice in surface science laboratories of studying single crystal materials of specific orientation in rigidly controlled environments. In these idealised conditions it becomes possible to study and compare the effects of each element of a surface, such as its steps, different surface planes and orientations individually. Thus allowing a knowledge of its structural, electrical and chemical properties to be systematically acquired.

Studying the effects of applying one material to the surface of another is not a modern practice. The observations of oil spreading across the surface of water provided the Babylonians with a less than scientific means of predicting the future. Bede's Ecclesiastical History (731 A.D.) records the use of oil to decrease the violence of water waves, an observation later undertaken more scientifically by Benjamin Franklin on a pond on Clapham Common. Advances towards the modern view of surface science began in the nineteenth century with the observation of the catalytic properties of platinum by Michael Faraday (1833); other contributions to the field were made by J.W.Gibbs in the thermodynamics of surfaces, I. Langmuir in vacuum technology, chemical adsorption and adsorption kinetics, together with the work of Davisson and Germer on wave-particle duality which led on to the development of Low Energy Electron Diffraction (LEED) in the 1960's. About this time the distinction was being made between contaminated and clean surfaces, the latter only being possible for most materials under Ultra High Vacuum (UHV) conditions. With the advent of the ion gauge in the mid 1950's and the transition from glass to metal vacuum chambers in the 1960's,

these conditions could be reliably produced and monitored. The systematic study of clean surfaces of known crystallographic orientation could then begin.

In the intervening years a number of techniques have been developed and applied, all of which involve the impinging of either electrons, photons, ions or neutral atoms or molecules on a surface and the subsequent detection of one of the same emitted after undergoing one of a number of possible interactions with the surface. All of these techniques are surface specific and when applied to periodic structures are capable of yielding information of the order of atomic dimensions. Small isolated or non-periodic features were not generally accessible and so when Binnig and Rohrer, working at the IBM research laboratories in Zürich, developed the Scanning Tunneling Microscope (STM) a great advance in lateral resolution was achieved. With sufficient mechanical stability so as to allow lateral atomic resolution and a vertical resolution better than 0.1Å an atomically sharp tip can be scanned in close proximity to the sample surface. By maintaining a constant tunneling current a contour map of the electronic surface can be produced allowing the electronic structure of small periodic and non-periodic features to be investigated. With slight modification scanning tunneling spectroscopy can be used to extract information about occupied and unoccupied electronic states at the surface of the material.

1.2 Aims of this project.

The first goal of this project was to build a vibration damping UHV chamber capable of housing a Scanning Tunneling Microscope (STM) and the support

techniques of Low Energy Electron Diffraction (LEED), Auger Electron Spectroscopy (AES) and Ultraviolet Photoelectron Spectroscopy (UPS) as well as their associated gas, water and power supplies. Secondly an STM UHV compatible head had to be designed and subsequently built at Warwick based on a piezoelectric scanning tube as the tip control mechanism. In order that the sample could be transferred from the manipulator arm in the sample preparation and preliminary analysis region of the chamber into the STM itself a novel sample exchange mechanism had to be designed and manufactured.

Testing and calibration of the instrument would then need to be carried out in air, but later under UHV conditions. The ultimate goal of the project was to use this home built STM to perform atomic resolution experiments to study adsorbate induced reconstructions of metal surfaces.

1.3 Format of the Thesis.

Before presenting and discussing the results of this project a number of chapters are dedicated to the description of techniques used and developments carried out in the production of the UHV compatible STM head. Following this introductory chapter is a chapter containing a brief overview of the theory of surface science techniques available on the apparatus.

Chapter three begins with an introduction to the STM and is followed by a review of the current status of semiconductor and metal tunneling microscopy. This is followed by a short description of STM derived instruments. The ability of the STM to be used as a spectroscopic instrument is then discussed.

Chapter four covers the basic theory of tunneling and goes on to describe the Tersoff-Hamann approximation for tunneling from a tip.

The fifth chapter begins with a review of STM designs, including examples of coarse tip-sample approach and vibration isolation techniques. This is followed by an account of the development and construction of the vacuum chamber and UHV compatible STM head and contains details of associated design problems, such as sample transfer, piezoelectric scanning tube selection and tip production.

Chapter six presents images obtained during STM development. The first of these are mica substrates coated with a layer of gold a few hundred Angstroms thick by vacuum deposition and imaged with a gold tip. These were imaged exclusively in air and show how vibration isolation was improved and electrical noise reduced. Later images of hydrogen terminated silicon samples show the vertical resolution of the STM to be capable of resolving single atomic steps. Some images of hydrogen terminated silicon and also images of copper were taken under UHV conditions and show that the step resolving capability is not lost when the STM is placed in the UHV chamber.

Chapter seven begins with a review of current knowledge of oxygen induced faceting and reconstructions of copper (110) and (100) surfaces and vicinal surfaces close to the (100) surface. A short section on the theory of oxygen adsorption on copper is followed by the presentation of the images of oxygen on copper (810). The images are discussed and a new model for the reconstruction of oxygen induced (410) facets on copper is proposed.

Background reading.

D P Woodruff and T A Delchar, Modern techniques of surface science, Cambridge solid state science series.

A Zangwill, Physics at surfaces, Cambridge University Press.

A W Adamson, Physical chemistry of surfaces, Wiley-Interscience publication, John Wiley and Sons Inc.

S R Morrison, The chemical physics of surfaces, Plenum Press.

Springer series in surface sciences, Springer-Verlag.

J F O'Hanlon, A users guide to vacuum technology, Wiley-Interscience, John Wiley and Sons Inc.

Chapter 2

Theory of Surface Science Techniques.

Contents

2.1 Introduction.

During the course of this work a number of experimental techniques have been employed in order to obtain the data discussed. This chapter is designed to give the reader an insight into the practical and theoretical aspects of these techniques and the extreme difficulties of operating in an Ultra High Vacuum (UHV) environment.

2.2 The UHV environment.

The environment is determined by the necessity to conduct experiments on atomically clean surfaces. If each molecule impinging on the material surface from the gas phase adheres to it, then at atmospheric pressure the surface would be completely contaminated within a very small fraction of a second. In order that this time period can be extended to one in which an experiment could be completed a reduction in the pressure of the surrounding gas phase is necessary. The pressure needed to allow a few hours of experimental time can be calculated quite simply from kinetic theory. An expression for the rate of arrival r of atoms or molecules

$$r = P(1/2\pi k_B T m)^{\frac{1}{2}} \tag{2.1}$$

at a surface, is given in equation (2.1) where k_B is Boltzmann's constant, m is the mass of the impinging particle, T is the temperature in Kelvin and P the pressure in Pascals. The above expression can be rewritten in a more convenient form with P in Torr and m substituted by the molecular mass M multiplied by the atomic mass unit to give equation (2.2)

$$r = 3.5\times10^{22}\left(\frac{P}{TM}\right)^{1/2} \tag{2.2}$$

By assuming T = 293 K and M = 28 (N_2 & CO) then the expression becomes approximately $r = 4\times10^{20}$ P molecules $cm^{-2}s^{-1}$. Assuming a sticking factor of unity, i.e. every atom that impinges on the surface sticks, then for a contamination level of a few percent over a time period of one hour a pressure of 10^{-8} Torr

is needed. Hence all UHV results given in this thesis were obtained with a base pressure below 5×10^{-10} mbar.

2.3 Cleaning surfaces in UHV.

Once in the vacuum chamber the surfaces of a material must be cleaned in order to remove both surface and bulk contaminants. One of the simplest ways of performing this is to cleave a crystal along a weak lattice plane, usually by mechanical means, but this unfortunately is not commonly possible and other cleaning techniques have to be employed. Semiconductors to be used for epitaxial growth are normally chemically cleaned in air before being cleaned by thermal desorption in the vacuum chamber. This removes most of the native oxides and surface contaminants to such a level as not to interfere with growth of the material being deposited. For some semiconductor materials this is not sufficiently thorough and a number of stages of ion bombardment, to remove surface contaminants, and annealing, to reorder the surface, must be undertaken. The annealing of the surface itself causes yet more contamination, as the elevated temperatures allow contaminants in the bulk of the material to migrate. These, unfortunately, migrate preferentially to the surface and so the cycle of bombarding and annealing must be carried out until the contaminants in the bulk have been sufficiently depleted. The level of contamination of the surface can be monitored by Auger Electron Spectroscopy (AES) and this technique was the one used to determine the cleanliness of the sample for this work.

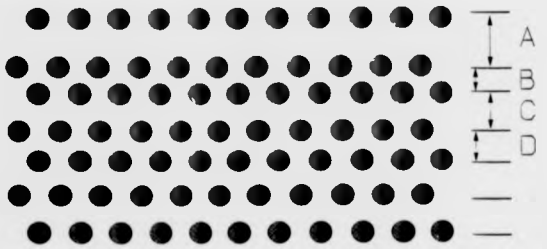

Figure 2.1: *The selvedge of a material showing relaxation of atomic layers extending from the surface into the bulk of the sample with variations in layer spacing A,B,C and D.*

2.4 2-D crystallographic structures.

Once properly cleaned and annealed the surface should adopt an ordered structure, this unfortunately is not a simple termination of the bulk and in most cases a reordering takes place. For the majority of surfaces this manifests itself as a relaxation of the atomic layers. The uppermost layer having no crystal layer to the vacuum side becomes drawn out away from the crystal whereas the next layer, being influenced by this displacement is drawn towards the bulk. This relaxation of layers diminishes with depth until the true bulk configuration is achieved. See figure 2.1. The disrupted region of the crystal between the true bulk structure and the vacuum is referred to as the selvedge. The question now arises as to

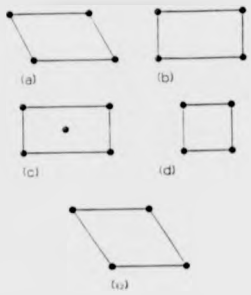

Figure 2.2: *The five two dimension Bravais-lattices. (a) Oblique, (b) rectangular, (c) centered rectangular, (d) square and (e) hexagonal.*

whether the arrangement of the atoms differs from that of the bulk material in the plane parallel to the surface and often this is the case. The periodicity can be expressed by five 2-D Bravais lattices. See figure 2.2. The most common variations of atomic structure between bulk and selvedge are ones of differing sizes of mesh, misalignment, rotation or simply atoms missing from certain locations, such as missing rows. The most general method for relating the size and shape of the adatom mesh or surface mesh to that of the substrate is the one proposed by Park and Madden (1968). This relates the primitive translation vectors of the substrate net a_{Sub} and b_{Sub} to those of the adsorbate or surface a_{Ads} and b_{Ads} expressed by the following relationship.

$$a_{Ads} = m_{11}a_{Sub} + m_{12}b_{Sub} \tag{2.3}$$

$$b_{Ads} = m_{21}a_{Sub} + m_{22}b_{Sub} \tag{2.4}$$

Here m_{ij} can be expressed as a matrix

$$M = \begin{pmatrix} m_{11} & m_{12} \\ m_{21} & m_{22} \end{pmatrix} \tag{2.5}$$

giving the following simple relationship between adsorbate and substrate mesh

$$\begin{pmatrix} a_{Ads} \\ b_{Ads} \end{pmatrix} = M \begin{pmatrix} a_{Sub} \\ b_{Sub} \end{pmatrix} \tag{2.6}$$

The matrix can also be used to determine the relative areas of the meshes by evaluating the determinant of M i.e. $|\ a \times b\ |$.

2.5 Low Energy Electron Diffraction (LEED).

The basic experiment which led to the development of LEED was carried out in the mid-1920's by Davisson and Germer, but the developments by Scheibner, Germer and Hartman in 1960 guided the way to the present LEED optics system. In this system electrons are used as a probe to determine the crystallographic structure of the surface. In order that this may be carried out successfully the wavelength of the probe must be comparable to that of the interatomic spacing. By using the DeBroglie wavelength $\lambda = h/p$ where h is Plancks constant and p is the momentum (mv) together with the energy $E = \frac{1}{2}mv^2$ we arrive at an expression for the wavelength given by

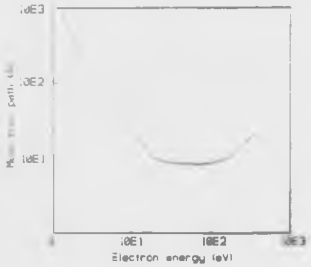

Figure 2.3: *The universal curve of the energy dependence of the electron inelastic scattering mean free path.*

$$\lambda = \frac{h}{(2mE)^{\frac{1}{2}}} \tag{2.7}$$

This gives a wavelength of 1Å at a kinetic energy of the electrons of 150eV. This is near the minimum of the universal curve of the energy dependence of the electron inelastic scattering mean free path, see figure 2.3, and when combined with the large elastic scattering cross section the depth of penetration of the incident electron is restricted to a few atomic layers. Thus LEED becomes a surface specific as well as a surface sensitive probe when energies between 20 and 500 eV are used. A schematic diagram of a LEED optics system is shown in figure 2.4. A mono-energetic beam of electrons leaves the electron gun and is incident on the sample. The electrons are scattered in well defined directions, dependent

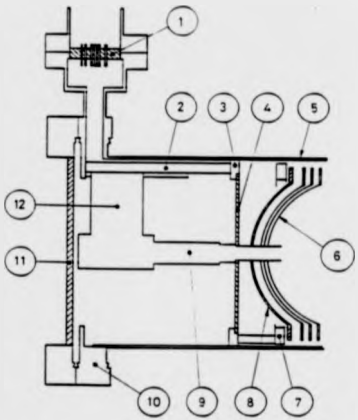

1. 11 PIN FEEDTHROUGH
2. SUPPORT ROD
3. MOUNTING RING
4. GLASS PLATE
5. MU-METAL CYLINDER
6. GRIDS (TWO OR THREE)
7. GRID MOUNTING RING
8. FLUORESCENT GLASS SCREEN
9. LEG 23 ELECTRON GUN
10. MOUNTING FLANGE
11. VIEWPORT
12. GUN SUPPORT STRUT

Figure 2.4: *Schematic diagram of rear view leed optics. (VG operating manual, Rear View LEED 640 RVL.)*

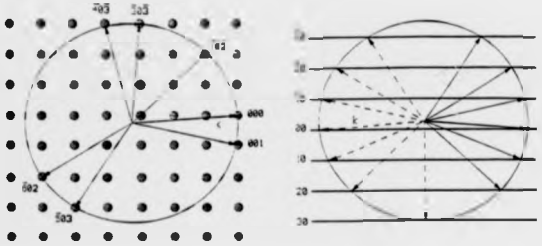

Figure 2.5: *Ewald sphere construction for (a) bulk and (b) surface. The incident wave vector k is labeled, possible scattered wave vectors are shown.*

on the crystal surface structure, due to interference phenomena. The grids G_1 to G_3 have retarding potentials applied so as to allow only the elastically scattered electrons to pass through. These are then accelerated by a 5kV potential onto the fluorescent screen, S.

The diffraction pattern observed on the LEED screen consists of a number of spots in an ordered array. This is in fact a projection of the surface reciprocal net and is best represented using the Ewald Sphere shown in figure 2.5. In reciprocal space the distance between two points is inversely proportional to the distance between the two corresponding points on the original lattice. For a two dimensional lattice the periodicity normal to the surface is infinite and thus the reciprocal lattice points are infinitely close in that direction leading to rods in

reciprocal space that are normal to the sample surface.

If these rods are drawn and the wave vector k is then added so as to terminate at the origin of the reciprocal net, the sphere of radius k superimposed will intersect the reciprocal lattice rods at points along the directions of the diffracted beams. Therefore this ordered array of spots will represent the surface crystallographic periodicity. If an overlayer of atoms is then added to the surface with periodicity exactly the same as that of the adsorbate then no change in pattern will be observed. However, if the periodicity of the overlayer is different then the LEED pattern will alter correspondingly.

The presence of regular steps on the surface changes the periodicity perpendicular to the line of the step edge and thus modifies the reciprocal lattice. The steps however have a periodicity of their own and will produce their own diffraction pattern, the origin of which will be offset by an amount dependent on the angle between the crystal planes and the step edge plane as shown in figure 2.6. As the diffraction pattern is in fact a Fourier transform, the diffraction pattern of the complete system will be the product of the two individual diffraction patterns and will therefore produce spots only where the maxima coincide. An example of this is given in figure 2.7 showing that the broadening of the rod maxima along with the intersection of the step maxima produces spot splitting.

A more mathematical approach can be applied by considering the conservation of energy and momentum. The incident and emerging electrons have wave vectors k and k' that are related by the following equations

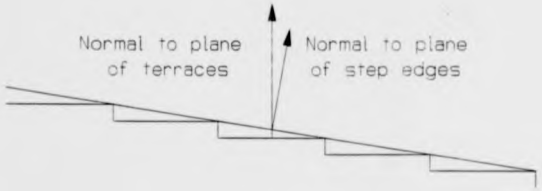

Figure 2.6: *A schematic of a stepped surface showing the difference in angle between the terraces and the overall surface.*

$$k^2 = k'^2 \qquad (energy) \qquad\qquad k' = k + g_{hkl} \qquad (momentum) \qquad (2.8)$$

where g_{hkl} is the reciprocal lattice vector i.e. $g_{hkl} = ha^* + kb^* + lc^*$. Because the crystal periodicity perpendicular to the surface is lost momentum is only conserved parallel to the surface so the conservation of momentum for the two dimensional system becomes

$$k'_{||} = k_{||} + g_{hk} \qquad (2.9)$$

If g_{hk} satisfies this equation then the Bragg condition for interference given in real space by $n\lambda = 2dsin\theta$ is satisfied and a diffracted beam is produced.

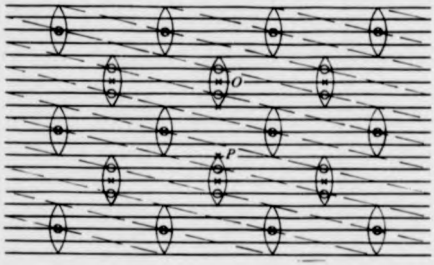

Figure 2.7: *The construction of the Fourier transform that yields spot splitting on the Cu(410) surface (after Perdereau and Rhead, 1971).*

If a and b are the primitive translation vectors of the two dimensional lattice then those for the reciprocal lattice are defined as

$$a^* = \frac{2\pi(b \times c)}{A} \qquad and \qquad b^* = \frac{2\pi(a \times c)}{A} \tag{2.10}$$

where c is the unit vector normal to the surface and $A = a.b \times c$.

As for the real space adsorbate and substrate lattice vectors the reciprocal space adsorbate and substrate lattice vectors can be connected by a transformation matrix, in this case M^*

$$\begin{pmatrix} a^*_{Ads} \\ b^*_{Ads} \end{pmatrix} = M^* \begin{pmatrix} a^*_{Sub} \\ b^*_{Sub} \end{pmatrix} \tag{2.11}$$

giving

$$a^*_{Ads} = m^*_{11} a_{Sub} + m^*_{12} b_{Sub} \qquad b^*_{Ads} = m^*_{21} a_{Sub} + m^*_{22} b_{Sub} \tag{2.12}$$

The matrices M for the real space and M^* for the reciprocal space are related by

$$M^* = M^{-1} \tag{2.13}$$

where

$$M^{-1} = \frac{1}{det} \begin{vmatrix} m_{22} & -m_{12} \\ -m_{21} & m_{11} \end{vmatrix} \tag{2.14}$$

and is the inverse transposed matrix of M. Thus by observing the relevant LEED pattern the periodicity of the real surface can be derived from the reciprocal lattice.

The instrument used for the LEED analysis was a Vacuum Generators rear view LEED optics VG 640 RVL.

2.6 Auger Electron Spectroscopy. (AES)

Accurate measurement of core level electron energies enable electron spectroscopies to be used to identify specific chemical species on the surface of a material. Auger Electron Spectroscopy (AES) is a non-destructive technique that employs the detection of Auger Electrons, named after Pierre Auger who first observed them in 1923. Their origin can best be described by the use of an energy level diagram, figure 2.8. In this process an electron is ejected from a core level by high energy electron bombardment, typically using an electron energy of about three times that of the binding energy, figure 2.9. The core hole, energy E_1, is then filled by an electron relaxing from a less tightly bound state in an outer shell E_2. The energy surplus is simultaneously removed by the production of an X-ray photon or by the ejection of a third electron from level E_3 of the atom, the latter being predominant for atomic numbers lower than Z=33. This ejected electron, the Auger electron, will be released with a kinetic energy that can be approximately given by equation 2.15.

$$K.E. = E_1 - E_2 - E_3 \tag{2.15}$$

The energy released by an electron falling from level 2 to level 1, $E_1 - E_2$, is transferred to an electron in level 3 which is then ejected losing an energy E_3 needed to escape the binding energy of level 3. This equation is only an

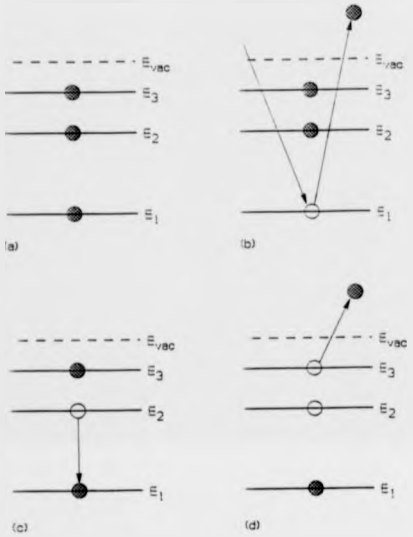

Figure 2.8: *Auger transition energy level diagram showing hole creation and subsequent electron transitions.*

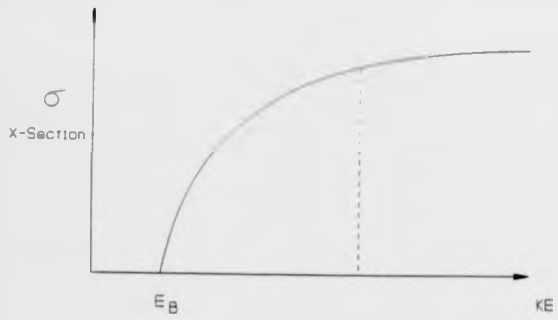

Figure 2.9: *Schematic of electron cross section showing it to be approaching maximum at 3 times the binding energy E_B.*

approximation, as the Auger electron is in fact ejected from an ionized atom and so has to overcome the effect of increased binding energy of a non neutral atom from a one-hole to a two-hole state. Again, very approximately this can be allowed for by substituting the binding energy of electron 3 with the corresponding energy of an atom of atomic number Z + 1, thus as electrons 2 and 3 are not distinguishable equation 2.16 gives a result of sufficient accuracy to allow clear identification of chemical species.

$$K.E. = E_1^Z - \frac{1}{2}\left(E_2^Z + E_2^{Z+1}\right) - \frac{1}{2}\left(E_3^Z + E_3^{Z+1}\right) \qquad (2.16)$$

The number of Auger transitions available for each atom depends on the number of electrons present. Clearly this technique can not be used on atoms

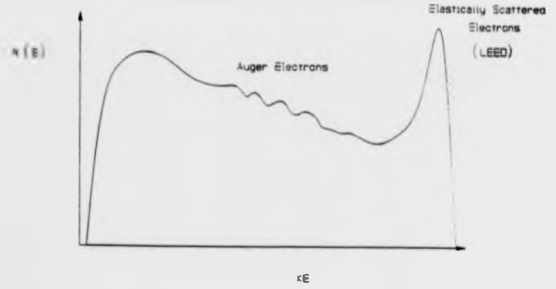

Figure 2.10: *Schematic diagram of number of electrons detected with increasing energy. The Auger electron peaks are exaggerated.*

containing fewer than three electrons, i.e. Hydrogen and Helium.

The detection of Auger electrons is not trivial as their number is small compared to the background of electrons emitted from the surface, figure 2.10. The small deviations in the energy spectrum can be enhanced by differentiation and a first derivative reveals the Auger peaks on a suitably levelled background, figure 2.11. Differentiation can be carried out by modulation of the sample potential and measuring only the modulated part of the signal current, thus resulting in the modulation of electron energy from E_O to $E_O+\Delta E$ (figure 2.12). The number of electrons between E_O and $E_O+\Delta E$ is proportional to the height of $N(E)$ at E_O this gives the required result. Mathematically this can be shown by substituting $\Delta E = k sin\omega t$ into equation 2.17 and rearranging.

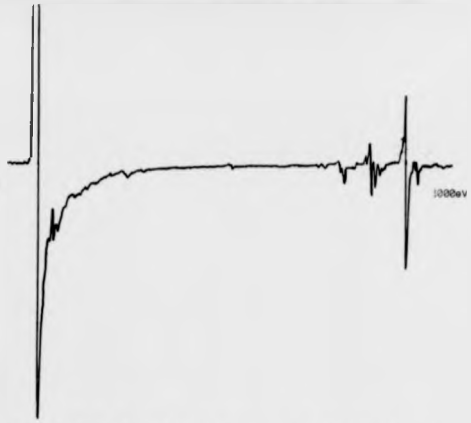

Figure 2.11: *Typical Auger electron spectra for clean copper.*

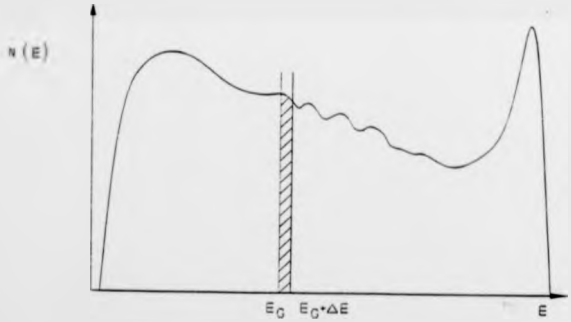

Figure 2.12: *Schematic diagram of number of electrons between E_O and $E_O + \Delta E$.*

$$I(E+\Delta E) = I(E) + I'(E)\Delta E + \frac{I''(E)\Delta E^2}{2!} + \ldots \qquad (2.17)$$

The result is a Taylor series in which if k is small then all elements containing k^3 and above can be ignored.

$$I = I_0 + \left[I'k + \frac{I'''k^3}{8} + \ldots\right] sin\omega t + \left[\frac{I''k^2}{4} + \frac{I''''k^4}{48} + \ldots\right] cos2\omega t \qquad (2.18)$$

The result is an equation which shows the second harmonic $cos2\omega t$ with the second derivative I''.

$$I = I_0 + I'ksin\omega t + \frac{I''k^2}{4}cos\omega t \qquad (2.19)$$

In the experiments reported here the voltage modulation applied to the sample was also connected to a lock-in amplifier as a reference for the signal. The equipment used for AES in this project was a VSW EG5 electron gun and a VSW HA50 Hemispherical Analyser controlled by a HAC 5000 controller. The lock-in amplifier and modulation source were a Brookdeal 402 and a Brookdeal 9472 respectively. The output signal from the lock-in amplifier could be connected to a chart recorder or alternatively imported directly into an analogue to digital converter in an IBM compatible PC.

2.7 Mass Spectrometry.

This thesis contains no direct mass spectrometry results, but the use of spectra proved invaluable in the attainment and maintenance of a leak free vacuum

chamber. Figure 2.13 shows a series of typical spectra obtained at three different vacuum conditions. These spectra give an example of the mass numbers expected at various pressures, the features to note are those of mass number 28, nitrogen and carbon monoxide, and a cluster of masses leading up to 18, water. These are very evident at 10^{-6} mbar but after baking the chamber for up to 48 hours at 130 degrees C these mass numbers have been notably reduced. The instrument used was a Vacuum Generators Micromass Q7 Quadrupole Mass Spectrometer capable of detecting partial pressures of the order of 10^{-10} mbar.

2.8 Ultraviolet Photoelectron Spectroscopy (UPS).

Photoelectron spectroscopy is a powerful tool for examining the energy distribution of the more loosely bound electrons in a surface atom. The theory of this technique is available in the literature (see background reading) and so the objective of this section is to provide the reader with a general overview of the topic.

The technique itself relies on the detection of an electron emitted due to the absorption of energy from an incident photon, see figure 2.14. The photons themselves are produced in an inert gas discharge lamp, generally providing He(I) radiation at 21.2 eV, He(II) at 40.2 eV or Ne(I) at 16.8 eV. Alternatively, a continuously tunable photon energy source such as a synchrotron may be used together with a monochromator. The low energy of the incident photons determines the electron energies that can be probed, in this case valence or shallow core level electrons of energies in the order of 5 to 20 eV. This technique however, unlike

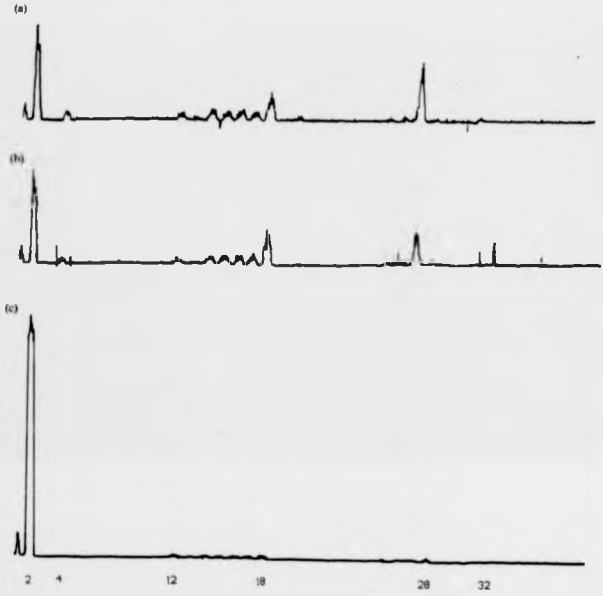

Figure 2.13: *Typical spectra obtained at three stages of UHV acquisition. (a) Air leak (b) Leak free and (c) Leak free baked system.*

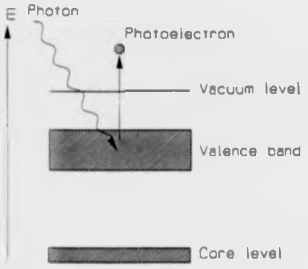

Figure 2.14: *Ultraviolet Photoelectron emission, the incident photon emits an electron from a loosely bound valence band level.*

Auger Electron Spectroscopy, is slightly less surface specific so both bulk and surface band structure contribute to the photoelectron spectra.

The Einstein equation gives an expression for the kinetic energies of emitted photoelectrons

$$K.E. = h\nu - E_B \tag{2.20}$$

where $h\nu$ is the energy of the incident photon, E_B is the photoelectron binding energy.

By detecting the kinetic energy of the electron a spectrum can be produced with peaks corresponding to binding energies E_B, see fig. 2.15.

Conservation of momentum plays an important role in photoemission from a solid. If the band structure is determined by electrons with specific energies E

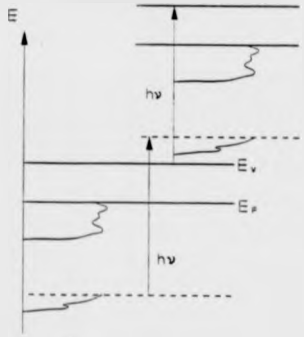

Figure 2.15: *Illustration of density of states relation to the kinetic energy spectrum for UPS.*

and momenta k then the conservation rule dictates that

$$E_f(k_f) = E_i(k_i) - h\nu \tag{2.21}$$

where f and i are final and initial states of the photoelectron. The momentum of the photon is negligible and can be disregarded, this gives us the relationship shown in equation (2.22).

$$k_f \approx k_i \tag{2.22}$$

The result is that transitions are only possible if $\Delta k \approx 0$. This is made possible as in a solid a change in reciprocal lattice vector G is not distinguishable from no change at all. The following also satisfies the $\Delta k \approx 0$ criterion

$$k_i = k_f + G \tag{2.23}$$

thus the ejection of an electron becomes possible by allowing the momentum recoil of the departing electron to be absorbed by the solid.

The instrumentation used for UPS analysis comprised a Vacuum Science Workshops UV10 photon source with a UV lamp power supply. The electron detection was performed by a VSW HA50 analyser and a HAC5000 electronic control system.

Bibliography.

D P Woodruff and T A Delchar, Modern techniques of surface science, Cambridge solid state science series.

A Zangwill, Physics at surfaces, Cambridge University Press.

A W Adamson, Physical chemistry of surfaces, Wiley-Interscience publication, John Wiley and Sons Inc.

S R Morrison, The chemical physics of surfaces, Plenum Press.

Springer series in surface sciences, Springer-Verlag.

J F O'Hanlon, A users guide to vacuum technology, Wiley-Interscience, John Wiley and Sons Inc.

Chapter 3

Review of STM, its Development and Uses.

Contents

3.1 Introduction and basic principles.

The field of STM has grown enormously in the last decade and studies of numerous materials in virtually all disciplines of science are now under way but it is in the field of surface science that the STM has proved to be an extremely powerful

tool. A complete review of STM work so far would be an enormous task and is covered in some detail by reviews to be found in the literature [10, 4, 25, 33, 34].

Surface science involves the investigation of the physical or electronic structure of material surfaces at an atomic or near atomic level. Generally this relies on the study of highly ordered single crystals enabling a relatively large area of the sample to be probed at a single instant using a diffraction technique. The data that result from this are an average for the whole of the surface and by definition do not yield specific information on any non periodic features present, such as defects. The STM provides a means by which non periodic features can be investigated and, indeed, allows the study of any conducting surfaces. The data produced is in real space and is especially useful in cases of large surface reconstruction periodicities or non-periodic features such as defects. The samples studied need not be single crystals.

The basic principle of the STM is very simple. A sharp tip is brought in to the proximity of a sample surface to allow a tunneling current to flow when a small voltage bias is applied across the gap, figure 3.1. This tunneling current is very sensitive to the tip-sample gap, and any alteration in gap width can easily be detected by the electronic control system. If the tip is scanned using piezoelectric transducers while the tunnel current is being kept constant by a feedback loop controling the vertical position of the tip, figure 3.2, a three dimensional map of the electronic surface can be obtained, figure 3.3.

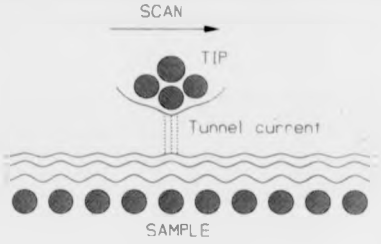

Figure 3.1: *Tip and Surface System.*

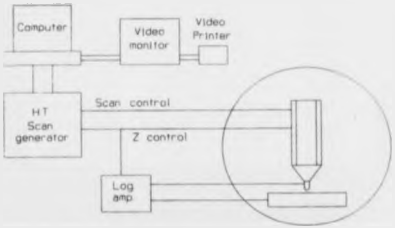

Figure 3.2: *Feedback loop controlling the z piezoelectric tube movement.*

Figure 3.3: *Three dimensional spatial image of the electronic surface.*

3.2 Development of the STM.

The STM was developed by Binnig and Rohrer in the early 1980's at the IBM research facility in Zürich, Switzerland but it is probably also fair to note the work of Young at the National Bureau of Standards, Washington D.C. in the early 1970's. Young developed an instrument for mapping the surface contours of a material by maintaining a constant current between tip and sample. The Topographiner as the instrument was known did not, however, operate in the tunneling region but in the high voltage bias region of the Field Ion Microscope (FIM). The general schematics of the topographiner were very similar to those of an STM, and had the bias been reduced and the vibration isolation been sufficient, then atomic resolution imaging may have been possible [55].

Totally independent of the work of Young, Binnig and Rohrer developed the STM. Their interest was in the spectroscopy of small surface areas, i.e. less than 100Å square, by using a sharp tip as one electrode. The idea then arose to scan the tip and the concept of the STM was born. The first instrument was magnetically levitated to isolate it from external vibrations and cooled to liquid nitrogen temperatures which helped reduce thermal drift and mechanical creep [7]. The ability to use piezoelectric materials as positioning devices was only established during the first experimental stages of this work. The problem of coarse and fine tip approach to the sample was solved by the use of crawling piezoelectric device or 'Louse'. The basic principles of this first instrument have been retained in all subsequent work although various techniques for data acquisition have been employed by other groups and will be discussed in the design chapter. [7, 8, 9]

3.3 First scientific results.

A number of images were produced by Binnig and Rohrer in an attempt to prove the resolution of their machine. The first of which were of $CaIrSn_4$ triple atomic steps with monatomic terraces [6], these were followed by images of single atomic steps on Si(111) [7, 8, 9]. These were images of sufficient resolution so as to allow surface reconstructions to be investigated, the first of which were of known periodicity such as the Au(110) (1×2), (1×3) and (1×4) reconstructions [11].

The first images to produce a significant advance to scientific knowledge were those of the Si(111)(7×7) reconstruction for which a suitable model had not yet been determined. The STM results showed the model proposed by Harrison [26] provided the best description of the images, although a later model by Takayanagi et al [47] ultimately became accepted. It must be noted that this model was obtained by taking into account the results of ion-channeling and transmission electron diffraction by Tromp [50, 51] as well as the STM data.

Some of the earliest work to be done on adsorbate systems was the measurements on the oxygen induced (2×1) reconstruction of Ni(110) by Baro [2]. This work was the first to show the ability of the STM to image adsorbates on a metal surface without itself altering the surface. Later work by Binnig, Fuchs and Stoll [5] showed that the presence of spikes in the data taken on the oxygen treated Ni(100) surface could be attributed to the movement of oxygen atoms under the tip during scanning. This phenomenon had been observed on their earlier work on Ni(110) and showed the possibility of observing the migration of adsorbates with consecutive scans. A series of images taken over time would allow the in-

vestigation of surface modifications, eg. adsorbate migration, island growth and step edge pinning.

The Si(111)(7×7) reconstruction has since been adopted by the STM community as the standard test of atomic resolution, although this is not a very rigorous test of the instrument's ability, as both amplitude and lateral scale of the surface features are relatively large; indeed they are amongst the largest features observed on atomically flat surfaces. Obtaining atomic resolution on metal surfaces is typically far more demanding for an STM instrument.

3.4 Atomic resolution imaging of different materials.

This section will discuss some of the early or most significant work produced with the STM on each of the major categories of sample ie. semiconductors, metals, adsorbate-semiconductor and adsorbate-metal systems. The objective is to give an overview of the types of study undertaken, and to provide only a few short examples of each surface science application.

The electronic characteristics of metal and semiconductor surfaces are significantly different. The directional nature of the bonds in semiconductors cause the electrons at the surface to be localised close to the atoms in the surface where they extend into the vacuum. The result is an electronic surface that has large perturbations extending a greater distance from the surface of the sample than metals. Electron orbitals in metals are less localised giving a much more even

electron distribution, leading to a reduction in perturbation extending out from the surface. The observation of atomic features on semiconductors is therefore not as demanding as obtaining atomic resolution on metal surfaces.

3.4.1 Semiconductor surfaces.

Silicon.

Following Binnig and Rohrer's work on the Si(111)(7×7) reconstructed surface [13] which was fitted to the Harrison model [26].Work by Hamers [23] on the spectroscopic imaging of the reconstructed surface showed the surface states to be resolvable and also revealed the electronic nature of the asymmetry between the two halves of the cell. An STM image of the reconstructed surface of Si(111) is shown in fig 3.4.

Research on other silicon surfaces has yielded information on the Si(100) (2×1) reconstruction, important because it is the most commonly produced silicon wafer orientation used in the semiconductor industry. Original models were the conjugated chain model suggested by Seiwatz [43] and later Chadi [14], the missing row model proposed by Harrison [26] and the dimer model of Levine [35]. The STM confirmed that dimers were present.

The 'ideal' termination of the Si(100) would be a (1×1) surface with each uppermost atom bonded to two atoms in the second layer which leaves two dangling bonds on each surface atoms. Levine proposed that to reduce the surface energy the surface reconstructs forming the dimers. The STM also confirms the presence of the (2×n) reconstruction of this surface where $6 \leq n \leq 10$. It was ini-

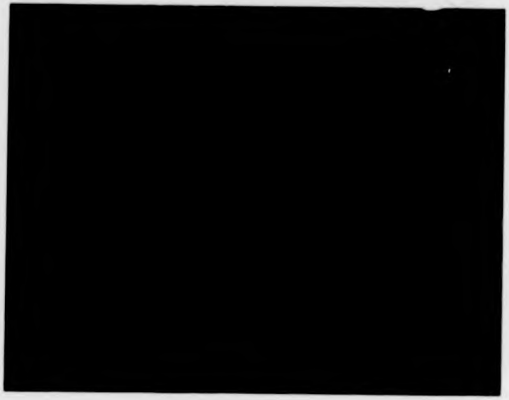

Figure 3.4: *Silicon (111) reconstructed surface (Perkin-Elmer literature).*

tially thought that the larger scale reconstructions were induced by nickel surface impurities, but later studies showed they could be formed by repeated bursts of annealing a clean surface at 1200°C.

III-V Semiconductors.

A number of groups are currently employed in the research of III-V semiconductors, and the STM has proved to be a useful tool for examining the surface states and species present in these materials. The ability of the STM to selectively image either the group III or the group V atoms, by adjusting the polarity of the bias voltage, allows two separate images of the surface to be acquired simultaneously by switching bias during the scan. If the two scans are then superimposed the relative positions of the group III and the group V atoms can be established. This technique was demonstrated by Feenstra et al [45, 46] on the GaAs(110) (1×1) reconstruction allowing the buckling angle of the Ga and As bonds to be estimated. This was one of the few cases in which the STM was used to determine the position of surface atoms in the direction perpendicular to the surface.

The ability of the STM to image the electronic surface of a material and not the physical corrugations was used to great effect in imaging the reconstruction of InSb [42]. The tunneling of electrons out of the lone pair of electrons in the antimony layer showed these atoms as bright spots, effectively making the upper layer of indium atoms invisible.

3.4.2 Atomic resolution on metal surfaces.

As mentioned above, the electron states in metals differ significantly from those in semiconductors. As a result of the delocalised nature of the electrons it has generally been assumed to be impossible to image individual atoms in a close packed metal surface with the resolution currently available on most STMs.

The larger features present on the surfaces of Au(110) (3×1) and (2×1) were imaged quite early in STM research by Binnig et al [11], but it was not until the work of Hallmark et al in 1987 [22] that atomic resolution on the Au(111) surface was achieved. Wintterlin et al [53] subsequently produced images of the Al(111) surface, these could only be produced when a very specific tip preparation was used. These results have the same unusual feature as graphite, i.e. they have unexpectedly large corrugations, (for the case of graphite up to 10Å [48] and for metals up to 1Å). It was suggested that these corrugations were a result of mechanical tip surface interactions, and arose from some form of deformation of the tip as it passed over an ion core. Later work by Chen [15] showed that a more likely reason would be the result of a d_{z^2} orbital located at the tip apex. This highly localised orbital, unlike an s state, increases the spatial resolution of the STM to the point at which close packed atomic surfaces become resolvable. The presence of d_{z^2} states on the tip is not necessary if they are present on the imaged surface itself.

3.4.3 Adsorbate coated surfaces.

Adsorbates on Semiconductors.

The adsorption of different materials onto the surface of a semiconductor alters the electronic state of the surface, sometimes inducing reconstructions. The STM is a very powerful tool for studying the changes in the electronic and physical structure of a surface. The adsorbed atoms or molecules generally allow the dangling bonds normally involved in dimer pairing to interact with the adsorbed species, resulting in a reduction in the surface energy, leaving the interface in a more relaxed state.

Si(111)(7×7) was one of the first semiconductor surfaces on which the adsorption of a metal was studied using the STM. When silver was adsorbed on this structure it was found to grow preferentially on the faulted region of the cell at lower temperatures, but at temperatures higher than 90°C the orientation of this adsorption is altered to form rings. At temperatures above 130°C the silver forms triangular shaped islands that completely cover the faulted region of the unit cell. At higher coverage the unfaulted region becomes covered with a silver overlayer.[49]

Another commonly studied adsorbate covered surface is that of Si(100) for the reasons mentioned above. The clean substrate has a well characterised (2×1) reconstruction. The adsorption of an alkali metal does not alter this. It was previously thought that linear chains of alkali metal atoms were orientated along the length of the dimer rows with each individual atom located in a pedestal site atop the dimer rows, Levine et al [35]. The STM images of Sakurai et al [39, 41],

however, showed that the linear chains of alkali metal actually ran perpendicular to the dimer rows. This was also observed for Ga and Ag on the Si(100)(2×1) surface. [37, 27]

Adsorbates on metals.

A number of different adsorbate on metal systems have been studied with the STM but of most relevance to this project are the studies involving copper. The oxygen induced reconstruction of Cu(100) surface to form Cu(100)-($\sqrt{2} \times 2\sqrt{2}$)R45°-O [28, 54] has been studied by Jensen. This was found to be of a missing row type reconstruction which has stabilising Cu-O-Cu chains along the [001] direction. The same stabilising Cu-O-Cu chains are found on the oxygen induced Cu(110)(2×1) structure [16, 29, 30, 32]. This topic is discussed in greater detail in chapter 7.

Work by Kern et al [31] on the Cu(110) surface showed a long range self organisation in the oxygen induced Cu(110)-(2×1)-O reconstruction. The Cu-O islands arrange themselves in long chains to form a supergrating along the [001] direction. The spacing of the chains is between 140 and 60 Å. This observation has not yet been explained fully.

In the sulphur induced step faceting on the Cu(11 1 1) surface Rousset [38] showed the two adsorbate structures, the p(2×1) and the c(4×2), existing simultaneously on the surface.

3.5 STM derived instruments.

A number of different instruments have been developed from the original STM design. Some are not true STMs but are derivatives of the original instrument. By far the most well known and widespread is the Atomic Force Microscope (AFM) but a number of other variations do exist.

The atomic force microscope (AFM).

The atomic force microscope has been developed to overcome the problem of imaging non-conducting materials. The AFM operates at a much reduced tip to sample distance relying on the repulsive atomic force of the two materials to deflect a fine cantilever kept under a constant force of approximately 10^{-8}N. The deflection of the cantilever is monitored as the sample is scanned beneath it. There are a number of forces involved in an AFM. The two most prominent being the attractive Van der Waals force, arising from fluctuating dipole moments of the molecules, and the repulsive Coulombic force, arising from the interactions between electron clouds of tip and sample atoms. A number of other forces may be applied to the system; if a voltage is applied to the tip then electrostatic charges build due to the capacitive nature of the non-conducting surface. Similarly if the materials used are magnetic then a magnetic force will be involved. Images obtained by this type of instrument are normally of a lower resolution than the STM [1].

3.5.1 Atomic manipulation.

The STM can be used to manipulate atoms or groups of atoms at the surface of a material in a number of ways. A number of uses for these devices have been suggested, such as the nanometer scale lithographic engineering of devices for the electronics industry, or the production of tiny devices for information storage.

The direct contact method involves the 'crashing' of the tip onto the sample in a controlled way so as to rearrange the surface layers. Another method for achieving lithographic features involves the deposition of a non-conducting layer onto the surface of the material. When the tip is then brought into tunneling range it must pierce this layer. The subsequent movement of the tip will then peel away strips of this layer to reveal the underlying surface.

The application of a voltage pulse to the tip can transfer material from the tip to the surface or vice versa. This allows the deposition of a specific material at any given point on the surface [21, 40]. Voltage application also alters the electronic nature of the region about the tip for the period of time for which the pulse is applied. This allows migration of material into and out of the tip region whilst the pulse is applied.[52]

By far the most satisfactory technique of atomic manipulation has been carried out by Eigler [19]. This involves the transfer of single atoms from sample to tip and back again by the application of a voltage bias. This allows the precise positioning of single atoms at a given point as well as the stacking of atoms to form clusters. This technique so far has only been performed at liquid helium temperatures, due to the mobility of most species at higher temperatures,

but with the marrying of the correct materials this might be achieved at higher temperatures. This same technique can be used as an atomic switch as the tunneling characteristics are different depending on whether the atom is on the tip or surface.[20]

3.5.2 Imaging in different conditions.

A number of STMs have been built that operate under very different ambient conditions to those of vacuum or air. These have included instruments operating under oil [18, 40, 36] water, solvents, saline solutions and in gases. These instruments have been built for specific tasks and are too numerous to mention in this thesis.

References

[1] G Binnig C Gerber and E Stoll, Surf Sci 189-190 (1987) p1

[2] A M Baro et al, Phys Rev Lett 52 (1984) p1304

[3] Barry Controls, Vibration, shock, noise catalogue.

[4] R J Behm, W Hosler, Surf Sci B

[5] G Binnig, H Fuchs and E Stoll, Surf Sci 169 (1986) pL295

[6] G Binnig, H Rohrer, Ch Gerber and E Weibel, Phys Rev Lett 49 (1992) p57

[7] G Binnig and H Rohrer, Helv Physica Acta 55 (1982) p726

[8] G Binnig and H Rohrer, Surf Sci 126 (1983) p236

[9] G Binnig and H Rohrer, Sci Am 253 (1985) p50

[10] G Binnig and H Rohrer, Rev Mod Phys 59 No3 (1987) p615

[11] G Binnig, H Rohrer, Ch Gerber and E Weibel, Surf Sci 131 (1983) pL379

[12] G Binnig, H Rohrer, Ch Gerber and E Weibel, Applied Physics Letters 40 (1982) p178

[13] G Binnig, H Rohrer, Ch Gerber and E Weibel, Phys Rev Lett 50 (1983) p120

[14] D J Chadi, J Vac Sci Technol 16 (1979) p1290

[15] C J Chen, Phys Rev Lett 65(4) (1990) p448

[16] D J Coulman, J Wintterlin, R J Behm and G Ertl, Phys Rev Lett 64 (1990) p1761

[17] B Drake R Sommerfeld J Schneir and P Hansma, Rev Sci Instrum 57 No.3 (1986) p441

[18] T Endo, H Yamada, T Sumomogi, K Kuwahara and S Morita, J Vac Sci Technol B9 No.2 (1991) p837

[19] D M Eigler, P S Weiss and E K Shwiezer, Phys Rev Lett 66 No.9 (1991) p1189

[20] D M Eigler, C P Lutz and W E Rudge, Nature 352 (1991) p600

[21] H P Hagan, A J L Ferguson, R J Turner, K W Smith, P Dawson and D G Walmsley, J Vac Sci Technol B 9 No.2 (1991) p879

[22] V M Hallmark, S Chiang, J F Rabolt, J D Swalen and R J Wilson, Phys Rev Lett 59 (1987) p2879

[23] R J Hamers, R M Tromp and J E Demuth, Phys Rev Lett 56 No.18 (1986) p1972

[24] R J Hamers, Ph Avouris, F Bozso. Phys Rev Lett 59 (1987) p2071

[25] P K Hansma and J Tersoff, J Appl Phys 61 No.2 (1987) pR1

[26] W A Harrison, Surf Sci 55 (1976) p1

[27] T Hashizume, R J Hamers, J E Demuth, K Markert and T Sakurai, J Vac Sci Technol A8 (1990) p249

[28] F Jensen, F Besenbacher, E Lægsgaard and I Stensgaard, Phys Rev 42 No.14 (1990) p9206

[29] F Jensen, F Besenbacher, E Lægsgaard and I Stensgaard, Phys Rev B41 (1990) p10233

[30] F Jensen, F Besenbacher, E Lægsgaard and I Stensgaard,in The Structure of Surfaces III, eds S Y Tong, M A Van Hove, K Takayanagi and X D Xie, vol.24, Springer Verlag Berlin (1991) p462

[31] K Kern, H Niehus, A Schatz, P Zeppenfeld, J George and G Comsa, Phys Rev Lett 67 No.7 (1991) p855

[32] Y Kuk, F M Chua, P J Silverman and J A Meyer, Phys Rev B41 (1990) p12393

[33] Y Kuk and P J Silverman, Rev Sci Instrum, 60 No.2 (1989) p165

[34] L E C van de Leemput and H van Kempen, Rep Prog Phys, 55 (1992) p1165

[35] J D Levine, Surf Sci 34 (1973) p90

[36] J Mou, W Sun, J Yan, W S Yang, C Lieu, Z Zhai, Q Xu and Y Xie, J Vac Sci Technol B. Microelectron Process Phenom 9 No.3 (1991) p1566

[37] J Nogami, S -I Park and C F Quate, Appl Phys Lett 53 (1988) p2086

[38] S Rousset, S Gauthier, O Siboulet, W Sacks, M Belin and J Klein, Phys Rev Lett 63 No.12 (1989) p1265

[39] Y Hasegawa, T Hashizume, I Kamiya, T Sakurai, H Tochihara, M Kubota and Y Murata Phys Rev B41 (1990) p9688

[40] R M Penner, M J Heben, N S Lewis and C F Quate, Appl Phys Lett, 58 No.13 (1991) p1389

[41] T Sakurai and T Hashizume, Proc Intern School on Surface Physics, March 20-30, 1990,Beijing, PRC, World Scientific Publ Co (1990)

[42] M O Schweizer, F M Liebsle, T S Jones, C F McConville and N V Richardson, Surf Sci (1992) In Press

[43] R Siewatz, Surf Sci 2 (1963) p473

[44] E Stoll, A Baratoff, A Selloni, P Carnevali. J Phys C. 17 (1984) 3073

[45] J A Stroscio, R M Feenstra and A P Fein, Phys Rev Lett 57 (1986) p2579

[46] J A Stroscio, R M Feenstra and A P Fein, Phys Rev Lett 58 (1987) p1668

[47] K Takayanagi et al, J Vac Sci Technol A 3 (1985) p1502

[48] J D Todd and J B Pethica, J Phys Cond Matt (1989) p9823

[49] St Tosch and H Neddermeyer, Phys Rev Lett 61 (1988) p349

[50] R M Tromp, Surf Sci 155 No.2-3 (1985) p432

[51] R M Tromp, Surf Sci 155 No.2-3 (1985) p441

[52] L J Whitman, J A Stroscio, R A Dragoset and R J Celotta, Science 251 (1991) p1206

[53] J Wintterlin, J Wiechers, Th Gritsch, H Hoefer and R J Behm, J Microsc 152 (1988) p423

[54] Ch Woll, R J Wilson, S Chiang, H C Zeng and K A R Mitchell, Phys Rev B 42 No.18 (1990) p11926

[55] R Young, J Ward and F Scire, Rev Sci Instrum 43(7) (1972) p999

Chapter 4

Theory of STM.

Contents

4.1 Introduction.

The ability of an STM to map the electronic structure of a surface topographically is dependent on electrons traveling across a narrow potential barrier to produce a tiny, but detectable, current. Classically electrons do not exist outside the surface of the conductor, but the quantum mechanical description of the electron as a wave leads to the result that the wave function does not terminate precisely at the potential barrier boundary, but penetrates slightly into it. There is therefore a probability of an electron existing outside the classical surface. This probability

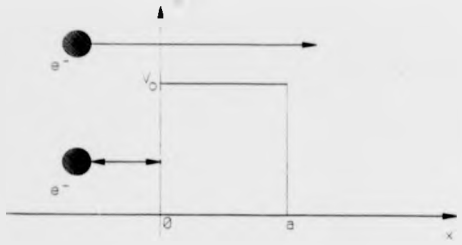

Figure 4.1: *Classical model of an electron approaching a potential barrier.*

decays exponentially over a short distance, but if two conducting surfaces are brought within a few Ångstroms of each other then there is a finite probability that electrons will flow between them.

Consider the classical approach of an electron with total energy E to a potential barrier of height V_0, see figure 4.1. It will have a probability of 1 of being reflected back into the $x<0$ region if $E<V_0$, and a probability of 1 of being transmitted to the $x>a$ region if $E>V_0$.

If, however, the $E< V_0$ case is described quantum mechanically then the penetration of the wave function into the barrier would allow the electron to be transmitted into the $x>a$ region if the barrier width was sufficiently narrow. In the region to the right and to the left of the barrier the electron has an eigenfunction that is one for a free particle. Within the barrier however the solution

to the time independent Schrodinger equation yields a different eigenfunction, which when matched to the free particle eigenfunction at the edge of the barrier will give finite values for the eigenfunction and its derivative at all points. The result is a function that, on reaching the edge of the barrier, does not terminate immediately but penetrates it in an evanescent manner. This penetration of the electron through the barrier is quantum mechanical tunneling. In performing this task, i.e. when the particle is in the region 0<x<a, it behaves purely as a wave, but on reaching the region x>a it behaves again as a detectable particle, see figure 4.2.

If a small bias voltage is applied to one of the conductors this penetration of the barrier, quantum mechanical tunneling, is increased preferentially in one direction. Thus, a potential gradient causes a net tunnel current to flow between the two electrodes.

4.2 Tunneling between planar electrodes.

Sommerfeld and Bethe [6] used the Wenzel-Kramer-Brillouin (WKB) approximation for the probability of barrier penetration of an electron for their early work on tunneling theory. They considered a rectangular potential barrier between two planar electrodes separated by an insulating layer, the metal-insulator-metal system. Later this work was simplified by Holm [2] whose work had been based on that of Kirschstein [3] in the low voltage case.

Simmon's approach [5] on the other hand, assumed a more generalised barrier, see figure 4.3, at the low temperature limit so that the thermal current could be

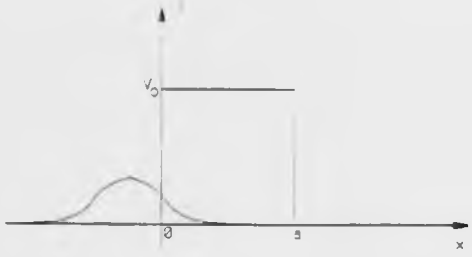

Figure 4.2: *Quantum mechanical model of an electron with wave function penetrating the barrier.*

neglected.

The penetration probability $D(E_x)$ of electrons through a barrier of width $s_2 - s_1$ at the Fermi level and of height $V(x)$ can be represented by

$$D(E_x) = exp\{-\frac{4\pi}{h}\int_{s_1}^{s_2}[2m(V(x) - E_x)]^{\frac{1}{2}}dx\} \qquad (4.1)$$

where E_x is the energy of the incident electrons in the x direction and is equal to $\frac{1}{2}mv_x^2$. From this probability an expression for the number of electrons that tunnel can be derived

$$N_1 = \int_0^{v_{max}} n(v_x)D(E_x)dv_x \qquad (4.2)$$

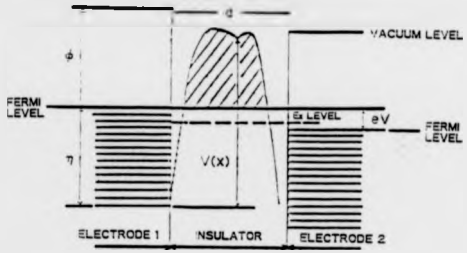

Figure 4.3: *Potential barrier for metal-insulator-metal tunneling.*

$$N_1 = \frac{1}{m}\int_0^{E_m} n(v_x)D(E_x)dE_x \tag{4.3}$$

Where E_m is the maximum energy of the electrons in the electrode and $n(v_x)$ is the density of electrons with velocity v_x. Equation 4.3 can be represented in polar coordinates by the expression

$$N_1 = \frac{4\pi m^2}{h^3}\int_0^{E_m} D(E_x)dE_x \int_0^{\infty} f(E)dE, \tag{4.4}$$

By a similar means the expression for the number of electrons tunneling in the opposite direction can be derived.

$$N_2 = \frac{4\pi m^2}{h^3}\int_0^{E_m} D(E_x)dE_x \int_0^{\infty} f(E+eV)dE, \tag{4.5}$$

By subtracting one from the other we can obtain an expression for the net number of electrons flowing through the barrier and hence the tunnel current.

$$J = eN = e(N_1 - N_2) \tag{4.6}$$

$$J = e\int_0^{E_m} D(E_x)(\zeta_1 - \zeta_2)dE_x \tag{4.7}$$

where

$$\zeta_1 = \frac{4\pi m^2}{h^3}\int_0^{\infty} f(E)dE_x$$

$$\zeta_2 = \frac{4\pi m^2}{h^3}\int_0^{\infty} f(E + eV)dE_x$$

This equation does not take into account the effects of the image force which is present when the interelectrode distance is small. If this force is taken into account then $V(x)=E_F + \varphi(x)$, where $\varphi(x)$ is the mean barrier height. This can now be substituted into equation 4.1 to give

$$D(E_x) = exp\{-\frac{4\pi}{h}(2m)^{\frac{1}{2}}\int_{x_1}^{x_2}(E_F + \varphi(x) - E_x)^{\frac{1}{2}}dx\} \tag{4.8}$$

By substituting 4.8 into 4.7 and neglecting higher terms, the low voltage limit gives the following expression for the tunnel current.

$$J = J_L\varphi^{-\frac{1}{2}}V\Delta s\, exp(-A\varphi^{-\frac{1}{2}}\Delta s) \tag{4.9}$$

where

$$J_L = \frac{(2m)^{\frac{1}{2}}}{\Delta s}\frac{e^2}{h^2}$$

$$A = \frac{4\pi\beta}{h}(2m)^{\frac{1}{2}}$$

$$\varphi = \frac{1}{\Delta s}\int_{x_1}^{x_2}\varphi(x)dx$$

The above equations yield a value for tunnel current for any shape of potential barrier of known average height.

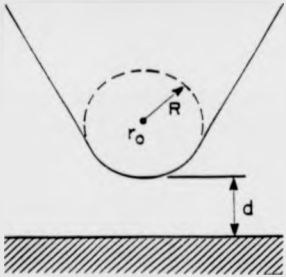

Figure 4.4: *Tersoff and Hamann tunneling geometry.*

4.3 The Tersoff-Hamann independent electrode approximation.

The earliest comprehensive work to take account of a non-planar electrode (a tip) was carried out by Tersoff and Hamann [7, 8, 9] and this is regarded as the first STM theory. The definition of a gap distance in STM is not a trivial one as the exact termination of the tip and surface can not be truly defined. Tersoff and Hamann assumed the gap distance to be that between a spherical tip, of radius R, and its closest approach to the surface, see figure 4.4.

Bardeen expressed the tunnel current as the following

$$I = \frac{2\pi e}{\hbar} \sum_{\mu,\nu} f(E_\mu)[1 - f(E_\nu + eV)] \mid M_{\mu\nu} \mid^2 \delta(E_\mu - E_\nu) \qquad (4.10)$$

In this equation the δ-function ensures that the electrons do not lose energy during tunneling (elastic tunneling), but this is not necessarily the case (see the inelastic tunneling discussion in the next section). The Fermi-Dirac function allows for the fact that electrons can only tunnel from filled to empty states, E_μ is the energy

of the state ψ_μ when not tunneling. The bias voltage causes the energy shift eV. The tunneling matrix element $M_{\mu\nu}$ between states ψ_μ of the probe and ψ_ν of the surface and can be expressed by

$$M_{\mu\nu} = \frac{\hbar^2}{2m} \int dS.(\psi_\mu^* \nabla \psi_\nu - \psi_\nu \nabla \psi_\mu^*) \tag{4.11}$$

In the low temperature limit and for small voltage bias (room temperature and below, and approx 10mV for metallic surfaces, respectively) the previous equation can be simplified to

$$I = \frac{2\pi}{\hbar} e^2 V \sum_{\mu\nu} \mid M_{\mu\nu} \mid^2 \delta(E_\mu - E_F)\delta(E_\nu - E_F) \tag{4.12}$$

The tunneling matrix element can be evaluated using the following asymptotic spherical form for the wave function of the tip

$$\psi_\mu = \Omega_T^{-\frac{1}{2}} c_t \kappa R e^{\kappa R} (\kappa \mid r - r_0 \mid)^{-1} e^{-\kappa |r - r_0|} \tag{4.13}$$

Ω_T is the probe volume and κ is the minimum inverse decay length for the wave function. The radius R is the local radius of curvature about the centre r_0 and

$$\kappa = \frac{(2m\phi)^{\frac{1}{2}}}{\hbar}$$

The wave function of the surface can be expanded along the same lines as that for the tip and can be expressed by the following

$$\psi_\nu = \Omega_S^{-\frac{1}{2}} \sum_G c_G exp\left[-(\kappa^2 + \mid \kappa \mid^2)^{\frac{1}{2}} z\right] exp(i\kappa_G.x) \tag{4.14}$$

where Ω_S is the sample volume and κ_G is the sum of the wave vectors along the surface $\kappa_\parallel$ and the surface reciprocal lattice vectors G.

$$\kappa_G = \kappa_\parallel + G \tag{4.15}$$

By substituting the expressions for the wave functions for the tip and the surface, the tunneling matrix element can be evaluated. If this is then expanded in terms of G the following result is obtained

$$M_{\mu\nu} = \frac{\hbar^2}{2m}\frac{4\pi}{\kappa\Omega_T^{\frac{1}{2}}}\kappa R e^{\kappa R}\psi_\nu(r_0) \tag{4.16}$$

This can now be combined with equation 4.12 to give

$$I = \frac{32\pi^3}{\hbar}e^2V\phi^2D(E_t)R^2\frac{e^{2\kappa R}}{\kappa^4}\sum_\nu \mid \psi_\nu(r_0) \mid^2 \delta(E_\nu - E_F) \tag{4.17}$$

where $D(E_t)$ is the density of states per unit volume of the tip. This formula states that the tunnel current is proportional to the density of states at the Fermi energy, evaluated at the tip. The summation gives the electron density evaluated at position r. Since

$$\sum_\nu \mid \psi_\nu(r_0) \mid^2 \delta(E_\nu - E_F) \simeq exp[-2\kappa_0(R+s)] \tag{4.18}$$

the current is proportional to $exp(-2\kappa_0 s)$.

This result has the major advantage of being able to be directly compared with an STM image. Tersoff and Hamann did this for the Au(110) (2×1), and (3×1) surfaces with good results [7]. The use of this formula has been regarded as sufficient to describe the theory of STM, as in most experimental cases the metal tips used are of tungsten or platinum. In the case of a metal tip the density of

states of the conduction electrons have an isotropic s/p component as well as the d electron. The d electron is localised near the core whereas the s/p electron has a large distribution outside the tip. This suggests that the tunneling contribution comes almost exclusively from the isotropic s/p electron and is indeed an adequate description for most STM work. The theory unfortunately does not hold for the imaging of close packed metal surfaces.

4.4 Inelastic tunneling.

If an electron loses energy whilst inside the barrier then inelastic tunneling occurs. Energy can be lost to vibrational states set up within the tunnel barrier. These vibrational states in turn provide another route by which an electron can tunnel, and effectively leads to an increase in the tunnel current. However the effect appears to be small; the overall tunneling current can be expected to increase by about 0.1% for a dipole interaction.

4.5 Atomic resolution tunneling from d_{z^2} states.

Investigations of metal surfaces by STM have yielded results that can not be explained by the Tersoff-Hamann theory. The atomic resolution images obtained on close packed metal surfaces should, by this theory, not be possible. This has led to Chen investigating the possibility that the extremely high resolution is indeed a result of the d electron being localized near the atom core on either the tip or the sample surface [1]. The density of states at the Fermi level of the d-

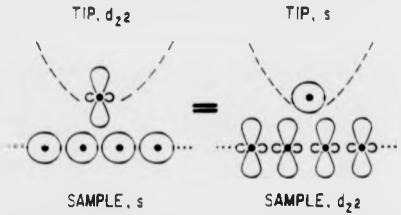

Figure 4.5: *Tunneling geometry for d-states, after Chen [1].*

band metals (eg. W, Pt and Ir) has a contribution of approximately 85% from d states. In addition tungsten has a tendency to form highly localised d_{z^2} dangling bonds on its surfaces. If one of these was to be present at the apex of a tip then the spatial resolution of the STM would be greatly enhanced.

The atomic resolution images can therefore arise from the d_{z^2} states being present on the tip or the surface. For a sample with s type states the tip will trace the charge density contour of a surface which has a d_{z^2} state superimposed on each atom of the surface. See figure 4.5

4.6 Scanning Tunneling Spectroscopy (STS).

Up to this point we have described the determination of tunnel current at or near the Fermi level by considering various models. If however the voltage applied to the sample, or tip, is increased to incorporate electronic states of the sample away from the Fermi level then the tunneling current may alter dramatically. The result is spatially resolved surface tunneling spectroscopy. By varying the tunnel

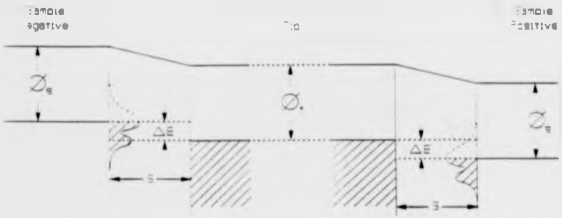

Figure 4.6: *Energy diagram for the tunneling of electrons through a barrier. The left hand side shows tunneling from the occupied states of a negative bias on the sample to the tip. The right shows tunneling from the tip to unoccupied states on the sample.*

voltage at each position of the tip during a scan the current voltage spectra for each specific point may be obtained. A derivative of this spectra yields peaks at high values of the local density of states (LDOS), such as surface states or resonances. The theoretical calculation of the tunneling current at voltages below the field emission threshold can be calculated from equations 4.10 and 4.11. The expression obtained by Selloni et al [4] is given in eqn. 4.19. It gives a formula for the differential conductance by assuming that the voltage dependence of the transmission coefficient through the barrier can be neglected relative to the voltage dependence of the density of states of the surface. The density of states of the tip is assumed to be sufficiently featureless and $T(V)$ is the transmission coefficient of the barrier at voltage V.

$$\frac{dI}{dV} = \rho(r, E_F + eV)T(V) \tag{4.19}$$

References

[1] C J Chen,Phys Rev Lett 65(4) (1990) p448

[2] R Holm, J Appl Phys 22(1951) p569

[3] R Holm and B Kirschstein, Z Tech Phys 16 (1935) p488

[4] A Selloni, P Carnevali, E Tosatti and C D Chen, Phys Rev B31 No.4 (1985) p2602

[5] J G Simmons, J Appl Phys 34 (1963) p1793

[6] A Sommerfeld and H Bethe, Handbuch der Physik, ed. H Geiger and K Schell (Springer-Verlag, Berlin) Vol 24(2) (1933) p450

[7] J Tersoff and D R Hamann, Phys Rev Lett 50 (1983) p1998

[8] J Tersoff and D R Hamann, Phys Rev B31 No.2 (1985) p805

[9] J Tersoff, Phys Rev B 39 (1989) p1052

Chapter 5

Design and Development of an Ultra High Vacuum Chamber and STM Head.

Contents

5.1 Elements to consider in the design of an STM.

This chapter sets out to describe the interaction between the elements of design, development and testing needed to produce a satisfactory instrument capable of producing verifiable results at atomic or near atomic resolution. A number of techniques for performing the main tasks involved in STM are listed.

1. The method of vibration isolation for STM and chamber.
2. The sample transfer from chamber manipulator to STM.
3. Coarse approach, the initial approach of tip to sample.
4. Fine approach, the secondary slower approach that allows the tip to enter the tunneling regime without crashing.
5. The method of scanning the tip over the sample surface.
6. Tip production for air and vacuum tunneling.
7. The drift of the tip.

Each of these are dealt with individually in this chapter along with a short review of possible alternative choices for performing each particular task. The

restrictions imposed by cost and in-house manufacturing capability, although important, are not really entered into in this thesis but should be borne in mind.

5.2 Vibration isolation.

5.2.1 Vibration isolation techniques.

One of the fundamental resolution limiting factors of an STM is the ability to reduce the vibration of the system to such an extent as to make the resulting mechanical stability of the relative position of the tip and sample better than the spatial resolution which the tip can be moved. For the STM a minimum useful resolution is related to the exponential variation of tunneling current with distance from the sample. A number of techniques for vibration isolation are available, ranging greatly in price and complexity, from large optical tables to simple spring hung devices. The most commonly used systems comprise either metal springs or organic material isolators such as rubber or viton. These materials are often used in the final isolation stage of the STM, as the properties they exhibit are beneficial if used correctly. Viton, in the dimensions typically used in STM work, has a high degree of creep, making it not ideal for STM use, but has a relatively high resonant frequency (approx. 100 Hz in the dimensions used for STM) and a high level of damping, making it very effective at shock isolation. The metal springs on the other hand have smaller spring constants and consequently a much lower resonance frequency (approx. 1 Hz.) These provide very little damping and so are usually used in conjunction with a viscous or magnetic

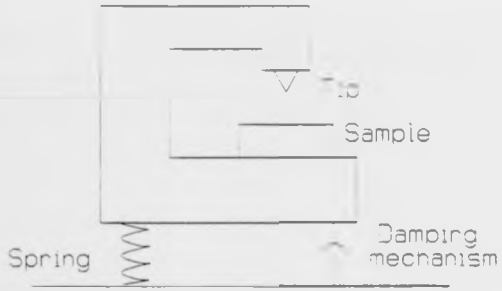

Figure 5.1: *Schematic of STM vibration isolation mechanism comprising both vibration isolator and damping mechanism.*

eddy current damping system [4, 5, 6], see figure 5.1.

5.2.2 Vibration isolation solution.

For most STM's there is more than one vibration isolation stage, and in our case there were three, the one present on the STM head itself and two that isolated the chamber and gas handling lines. The frequencies most critical in causing noise can be calculated roughly by considering the required scan rates to be as follows. If a scan time of approximately 0.03 seconds per line is assumed, then frequencies of 30 Hz would produce one vibration cycle per line, and would not coincide with the periodicity of the sample imaging. At the high frequency end of the region to be damped, 256 data points could reasonably be expected to

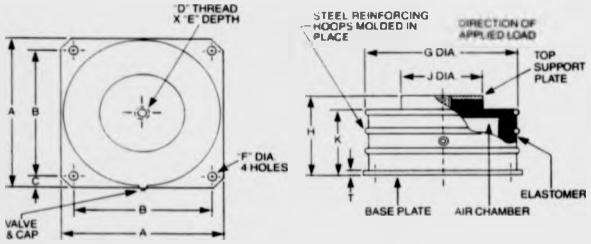

Figure 5.2: *Inflatable isolators used as vibration control (Barry Controls Manual).*

give alias free data on 50 features, that is a frequency of 2kHz. Thus to ensure that the image contains only data from the sample and not from vibrations good damping is required in the frequency range of a few Hz to a few kHz. We take this to be approximately from 10 Hz to 10 kHz.

The vibration isolation devices that most closely fitted these criteria, along with those mentioned in the introduction to this chapter, were individually inflatable isolators produced by 'Stable Level', see figures 5.2. and 5.3.

Due to the hostile environment in which the STM was to operate, i.e. in a shared laboratory on the third floor of a physics building, it was decided to use two stages of vibration isolation. The inner stage would hold only the vacuum chamber and UHV pumps and be connected by flexible bellows to an outer stage holding all of the gas handling lines. This in turn was connected to the rotary

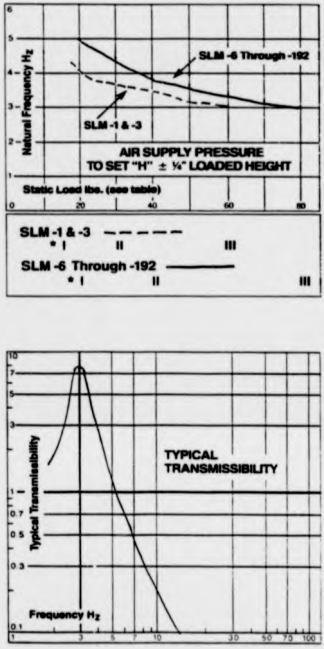

Figure 5.3: *Frequency response of Stable Level isolators (Barry Controls Manual).*

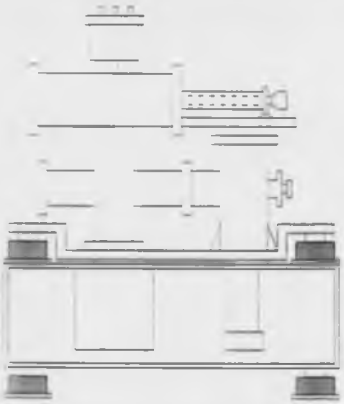

Figure 5.4: *Schematic of vacuum chamber and vibration isolation.*

pumps via rubber hoses. See figure 5.4. When built the chamber had an oscillation frequency of less than 5 Hz. The upper end of the damped region proved to be less easy to determine, because it was not possible to drive the whole system at a high frequency.

5.3 Design of vacuum chamber and gas lines.

A prerequisite for the STM was that the sample face was to be positioned horizontally, this resulted from the design of the initial STM, which was planned to be produced by Warwick University's Microengineering Department. Unfortunately the method of tip drive to be used [7] for this STM proved troublesome to produce and it became clear that the rate of development of the Engineering De-

partment design was not compatible with the timescale required in this project. This initial orientation constraint also dictated that the central axis of the vacuum chamber and the manipulator would need to lie horizontally. For ease of pumping the vacuum chamber needed to be kept as small as possible with large bore pumping tubes. A minimum travel of 240mm on the manipulator would be needed in order to allow transfer of the sample from the surface characterisation position, through the preparation position to the STM itself, see Figure 5.5. The characterisation position was located centrally with the LEED facing the operator; the hemispherical analyser (HA50) which was large and heavy was mounted above the chamber in order to keep the centre of gravity of the HA50 in line with that of the chamber. The electron gun, UV lamp and mass spectrometer were therefore placed at the rear of the chamber so as to form a vertical ring of characterisation instruments around the chamber.

A further feature of the Engineering Departments STM head is that it requires the use of permanent magnets in the scanning mechanism, leading to stray magnetic fields that were not compatible with the electron diffraction and spectroscopy instruments. It was therefore decided to keep the characterisation position as far from the STM as possible, and contained within a μ-metal shield, for this reason the sample preparation position was placed in between. The ion gun was located adjacent to, and at a small angle to, the LEED in order to prevent any sputtered particles from being deposited on the LEED optics, and the sample heater filament placed opposite.

With the location of each piece of analysis equipment on the chamber finalised,

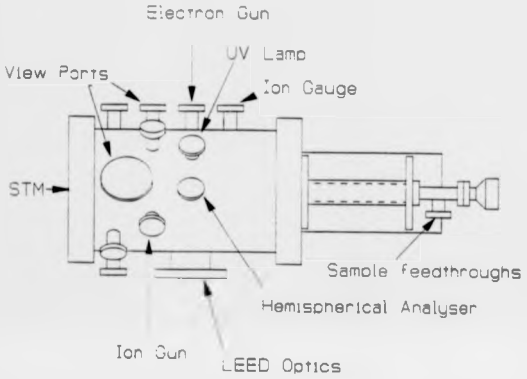

Figure 5.5: *Schematic diagram of vacuum chamber showing relative positions of analytic instruments.*

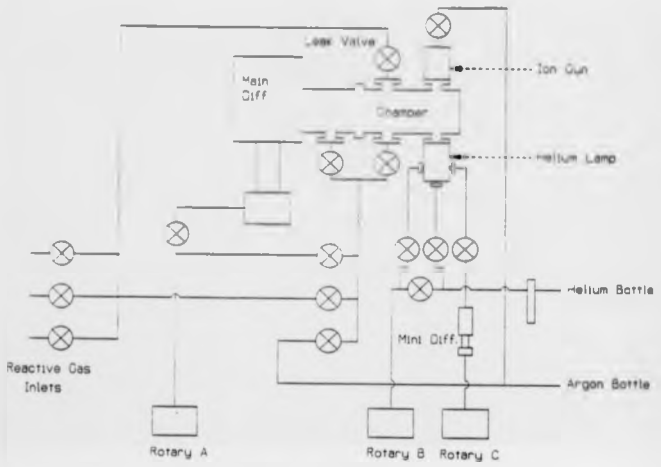

Figure 5.6: *Schematic of gas lines and pumping roots.*

it was then possible to design the gas, water and electricity supplies needed to run each of them. The main body of these supplies were to be positioned on the outer stage of the two stage antivibration system and connected by flexible bellows to the inner chamber stage.

All gas lines were arranged so that they could be diffusion pumped and baked, thus ensuring a high gas purity for both sample cleaning and reactive gases; a schematic of the gas lines is shown in figure 5.6.

5.4 Sample transfer.

5.4.1 Sample transfer techniques.

For general surface characterisation by LEED, AES etc., it is necessary to mount the sample on a rigid manipulator. However to prevent vibrations being transmitted to the STM whilst in use, there must be no contact between the sample and the chamber. This demands the use of a transfer mechanism that is capable of exchanging the sample and stub between the manipulator and the STM, reliably and with as little difficulty as possible. Many sample transfer mechanisms that are currently available make use of two or three individual rotary or linear drives to perform the exchange, and as a result are difficult to use effectively in a UHV system. The majority of these techniques involve the gripping of a sample stub by means of one or more leaf springs. This is difficult to do in UHV with the lack of tactile responses. In order that the sample is transferred in the desired direction the motion of the STM and manipulator sample holders must be at 90 degrees to each other, this demands alignment in two directions, see figure 5.7. In an attempt to make the transfer of samples simple to use, a novel one dimensional motion sample exchange mechanism needed to be developed.

5.4.2 Sample transfer mechanism.

With the objective of producing a single drive sample transfer device that would need no locking device, and no transfer arm other than the main sample manipulator, a novel transfer mechanism was designed. This involved the use of

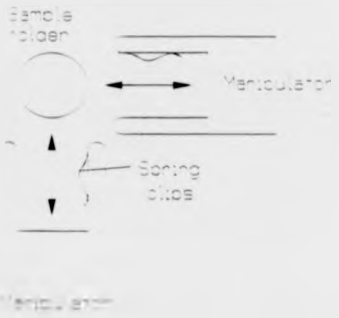

Figure 5.7: *Schematic diagram of sample transfer requiring 2-D alignment.*

tungsten leaf springs capable of alternately releasing and retrieving the sample holder without outside influence, see Figure 5.8. By driving the manipulator forward the sample is introduced to the STM; the leaf springs in the STM then pass under the leaf springs of the manipulator and rise over the wings of the holder, effectively gripping the sample holder. Withdrawing the manipulator completes the transfer. To remove the sample holder from the STM, the manipulator is simply driven into the STM again and the process is reversed, allowing the leaf springs of the manipulator to pass under those of the STM and over the sample holder wings; now withdrawal of the manipulator removes the sample holder. Thus with each approach of the manipulator to the STM, the sample holder is alternately deposited and retrieved.

The transfer of sample to the STM requires the disconnection of electrical

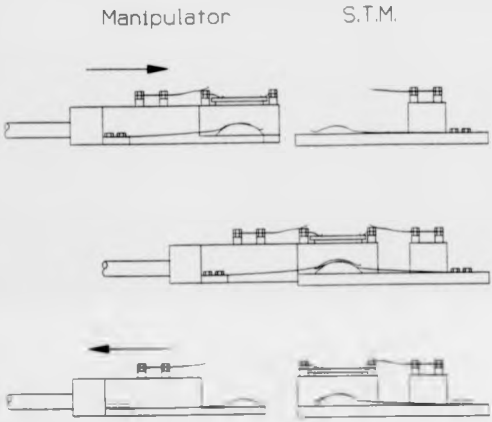

Figure 5.8: *Sample transfer mechanism showing sample stub transfer from manipulator to STM.*

contacts to the manipulator and reconnection on the STM to carry the tunneling current. Electron bombardment was used for heating the sample, but, in order to reduce the number of electrical connections to the sample stub, the heater filament was mounted independently on a fixed flange on the vacuum chamber. The result was a heater that needed the sample to be moved toward it, this reduced the freedom of the operator to select the heating location. The advantage of this arrangement, however, was that it reduced the number of sample connections and also removed the filament from the sample stub, avoiding additional possible vibrational problems when in the STM.

The remaining electrical connections to the sample, i.e. two thermocouple connections and a sample current connection, were made via tungsten leaf springs that engaged and disengaged automatically during sample stub transfer, see figure 5.9.

5.5 Tip to sample approach.

5.5.1 Tip to sample approach mechanisms.

One problem in STM is to devise a method of tip approach to the sample which covers the range between that viewable by eye (coarse approach $\sim$ mm) and that which can be detected electronically (fine approach $\sim$ nm). There are three main ways of performing the coarse and fine approach of the tip to sample. The first is by use of piezoelectric drivers and clamps, the second by means of lead screws and levers, and the third by means of differential screws.

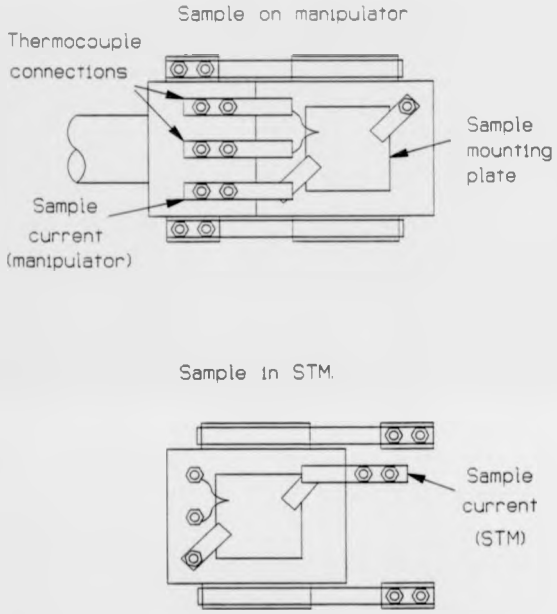

Figure 5.9: *Electrical connections to sample for both manipulator and STM.*

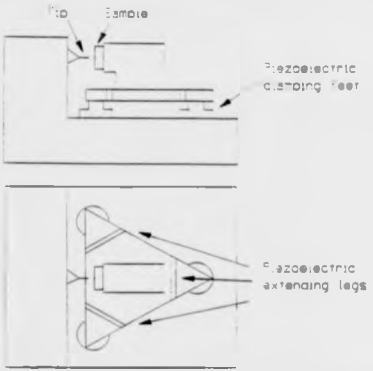

Figure 5.10: *Schematic of "louse" piezoelectric translator*[7].

One of the earliest techniques was the use of a piezoelectric "louse", so called because of its crawling action along the surface of a plate, see figure 5.10. The three piezoelectric feet on which the tip holder is mounted are clamped and released in conjunction with leg extensions that allow the whole of the louse to crawl at a predetermined rate toward the sample. This one system performs both coarse and fine approach. A later development in piezoelectric approach mechanisms, the inchworm, incorporated two annular clamping piezos, one at each end of a rod, separated by a piezo tube that could be extended along the length of the rod. By employing the correct sequence of clamping and extension, the tip (or sample) attached to the end of the rod could be brought within tunneling range without crashing. See figure 5.11.

The use of levers driven by a lead screw, see figure 5.12, allows a rotary motion

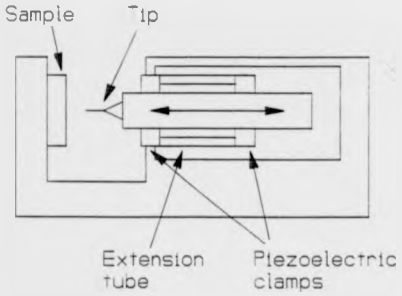

Figure 5.11: *Schematic diagram of Inchworm type tip to sample approach mechanism.*

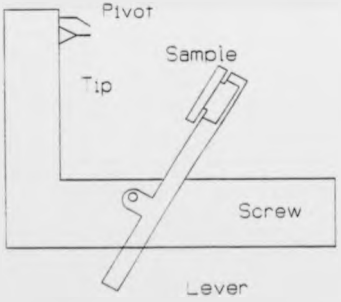

Figure 5.12: *Lead screw and lever type approach mechanism, after Demuth.*

to be translated into a linear approach. This enables up to a 100 to 1 reduction in the motion of a coarse approach and can be reduced even further in the fine approach to approximately 5000 to 1. This can allow a fine approach of as little as 500 Å per revolution of the lead screw. The third technique uses differential screws to alter the rate of advancement of a drive. In this case separate drives are usually necessary for each of the approach regimes. It also becomes necessary to observe the tip very closely on coarse approach to ensure that it approaches as close as can be determined optically without crashing.

5.5.2 Coarse and Fine Tip to Sample approach.

The initial constraint of a horizontal sample implies a vertical downward pointing tip, which is consistent with a tube scanning device sitting on the differential screws held only by gravity. The differential screws are thus mounted vertically. A three point kinematic mount was decided upon, each leg of which terminates with a ball bearing. The stationary leg located in a cone shaped socket, the coarse drive into a "V" shaped slot and the fine drive on a flat plate. Each contact point was of polished silver steel, see figure 5.13. The differential screws had 15 rotations for a travel of 3 mm for the coarse and 15 rotations for a 1.5 mm travel for the fine. These in turn are reduced by the ratio of drive-tip and drive-stationary mount distance; for the coarse movement this ratio is 1:2, and for the fine movement a ratio of 1:10 was used. This gave a tip movement of 0.1mm for the coarse movement and 0.0125 mm for the fine movement per 360 degree rotation of the appropriate drive. Assuming an accuracy of only 10 degrees in

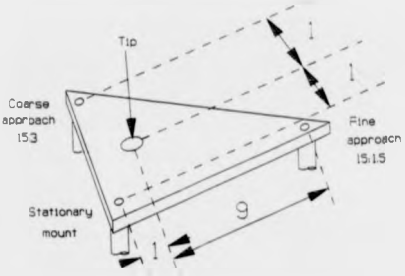

Figure 5.13: *Kinematic mount showing differential screw ratios and lever ratios.*

rotation enables a fine approach within 0.3 μm, well within the piezoelectric tube vertical displacement limit of 1.6 μm. Small springs attached to the differential screws prevented backlash, see figure 5.14.

The three point kinematic mount was integrated into a cradle design in which the STM could be kept vibrationally damped from the mounting bracket on the flange. The damping for this was achieved by stacking alternate layers of 2mm diameter viton 'O' rings and stainless steel plates. The differential screws protruded through the mounting plate and could be decoupled from the drive rods by backing off the simple rod and pin linkage. The initial design comprised of one rod and pin decoupling mechanism per drive screw located between the bevel gears and the rotary feedthroughs. The bevel gears were therefore incorporated into the tip sample mechanical loop. On modification to reduce noise, see chapter

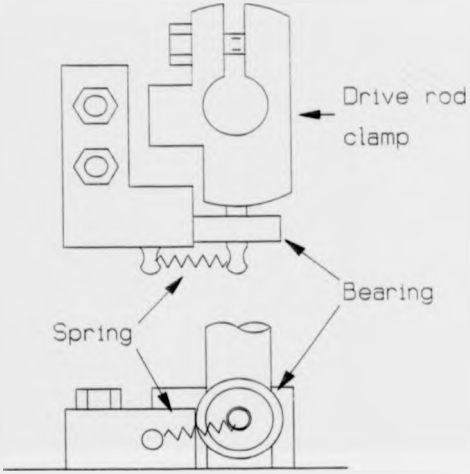

Figure 5.14: *Antibacklash device attached to differential drive rods. The springs keep the differential drive rods tight against the differential thread mechanism therefore avoiding slack.*

6, a second rod and pin decoupling point was added between the bevel gears and differential screw drives, see figure 5.15.

To aid coarse approach a pair of binoculars of 15 × magnification, and a pair of mirrors, gave the operator a view of the tip-sample region. When the tip and its reflection in the sample surface are just visibly separate the coarse approach can be decoupled and the fine approach begun. This fine approach could be monitored by the sample current, the approach being halted when a tunneling current was detected; the fine approach mechanism could then also be decoupled.

A clamping mechanism to be used for holding the stage steady during sample transfer and coarse approach was fitted centrally on the STM stage. The lever action was translated into a downward clamping mechanism by use of a phosphor-bronze quadrant, see figure 5.16. When not in use, the clamping device was completely decoupled from the damped stage.

5.6 Tip scanning.

5.6.1 Tip scanning techniques.

The fine control required for tip scanning is almost exclusively performed by means of piezoelectric drives. These are typically driven by voltages in the range of ±200 volts.

A number of piezoelectric ceramics are available that are used as electromagnetic transducers in other scientific and commercial fields, and so commercial devices can be selected with piezoelectric properties chosen to match those re-

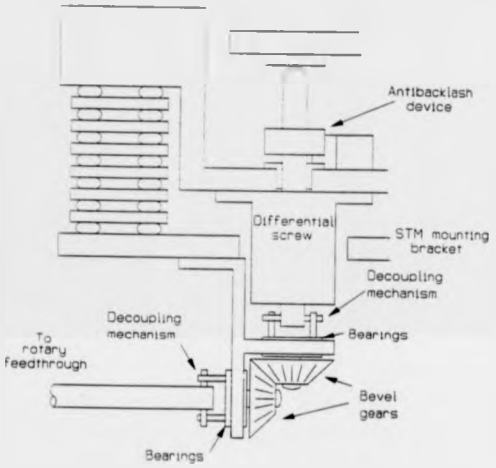

Figure 5.15: *Illustration of relative positioning of each of the elements involved in the differential screw tip approach mechanism.*

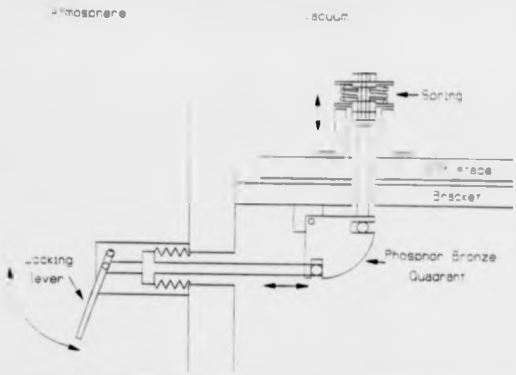

Figure 5.16: *Clamping mechanism to secure STM during sample transfer.*

quired for STM use. The most commonly used material is lead zirconate titanate (PZT) which has high sensitivity, permittivity and good time stability, (i.e. little creep). There are two main piezoelectric tip drive mechanisms. The first consists of three piezo blocks mounted orthogonally that perform the X,Y and Z motion separately, see figure 5.17. This method has the potential disadvantage of being unstable due to the three separate mounts. By contrast, a tube scanning device requires only one mounting point and the overall head design becomes more compact. The tube mechanism is made of a single piece of PZT polarized in a radial direction so as to produce a length extension for a given voltage differential across the tube walls, see figure 5.18. For the scanning mechanism to work, the electrodes on the tube must be segmented radially each arc of approximately 85°-90° along its length. The stripes are made of between 25 and 75 μm thick

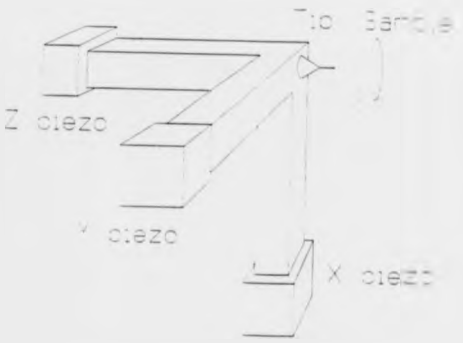

Figure 5.17: *Orthogonally mounted piezoelectric tip actuator.*

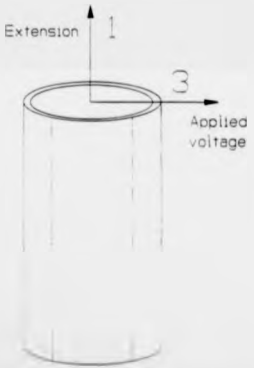

Figure 5.18: *PZT tube showing radial polarization.*

Figure 5.19: *Segmented PZT tube with separate z electrode.*

electrodeposited nickel.

There are a number of ways of producing a scanning motion and these depend on the orientation of the voltages applied to the stripe. If the electrodes are also segmented so as to produce a ring at the upper region of the tube this can then be used as a Z drive and the X an Y motion produced by the application of voltages to the lower segments of the tube, see figure 5.19. The actual deflection arises from the elongation of one side of the tube relative to the other. This can be achieved by applying a positive voltage to the outside of one of the stripes (+X) with an equal and opposite voltage to the stripe opposite (-X) while the centre of the tube is kept electrically grounded. The Y deflection is carried out in a similar way. Alternatively, instead of applying the Z voltage to a separate electrode it may be superimposed on all four of the translational drive stripes, see figure 5.20.

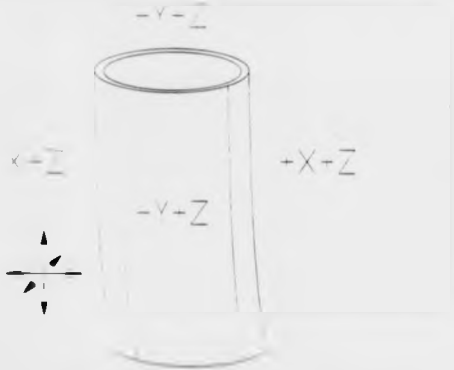

Figure 5.20: *PZT tube with Z voltage superimposed onto the X and Y electrodes.*

5.6.2 Tip scanning solution, the piezoelectric tube.

As it had been decided to use a piezo tube scanner to drive the STM, the electronics needed to control this had to be obtained. An agreement was entered into with W A Technology of Cambridge whereby they would modify their STM electronics controllers from a cartesian piezo block system to one for a tube scanning driver. In exchange for any benefits arising from the development of the STM head itself they would supply information and assistance in its manufacture.

The tube chosen was a PZT-5A produced by EBL Company, East Hartford, Connecticut. This tube has the characteristics of approximately 100 Å/V deflection in X and Y with a Z extension of approximately 40 Å/V [2]. This would allow a scanning area of around 8000 Å square if ±40 volts were applied to X and Y and a vertical range of 16000 Å with a voltage of ±200 volts to Z.

5.7 Tip production.

5.7.1 Tip production techniques.

In order that high resolution images can be obtained the tip must be sufficiently sharp so as to allow tunneling to occur only from the end atom. The production of tips for STM work has not yet been perfected to the level where a simple set of procedures will guarantee a tip capable of producing images at atomic resolution and the methods employed by differing groups are many and varied.

The most common method of producing tips for use in air is to simply cut wires of the appropriate material with wire cutters or a razor blade. For tips that are to be used in vacuum the most common technique is that of electrochemical etching. This can be carried out in a number of ways, an excellent review of these techniques is given by Melmed [3].

5.7.2 Tip production methods used.

A series of experiments were carried out to try and determine the best method of tip production, but an element of trial and error was also involved in producing the recipe. This has resulted in a technique for which the true physical reasons for each step are not fully understood.

In the initial stages of development the STM was used in air and so the tips needed to remain clean under atmospheric conditions. The most obvious material to use for this purpose is gold, however, other materials such as platinum-iridium (90:10) alloy can also be used. Tips can be cut from wire with a razor blade on a

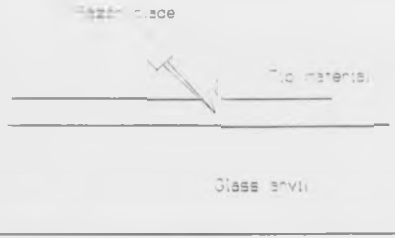

Figure 5.21: *The simplest form of tip production, cutting a soft wire with a razor blade.*

glass anvil, see figure 5.21. These tips, however, do not produce atomic resolution images as they are not sharp enough, and the mobility of the atoms at the apex precludes the production of a stable tunneling microtip.

For scanning in UHV a number of other materials can be used. The most common of these is tungsten, which when electrochemically etched in 1 molar solution of either sodium hydroxide or potassium hydroxide will produce stable, atomically sharp, tips. There are a number of techniques employed for tip production each of which determines the success rate of tips capable of producing atomic resolution.

If a tungsten wire is coated with an insulating lacquer leaving a bare section of wire for the etch then the gradual necking of the wire will reduce its strength

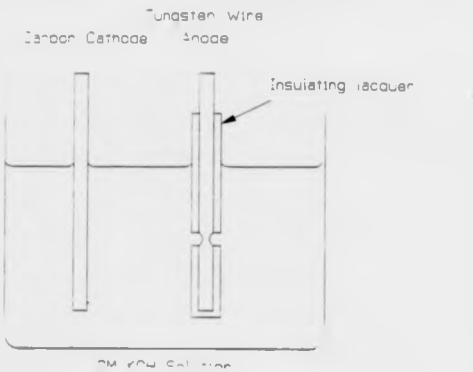

Figure 5.22: *Production of tips by etching uncoated region of wire.*

and so the weight of wire hanging will eventually cause it to fracture, see figure 5.22. Examination of these tips in an electron microscope showed typical fracture of the wire and poor quality tips, see figure 5.23. The diameter of the wire left hanging can be reduced by placing bare tungsten wire in a similar solution to the one above allowing 10-15mm of wire to penetrate below the miniscus. The rate of etching is faster at the miniscus and so the wire will neck at this point, however, the bare wire in the solution will also etch and the resulting reduced weight of wire that causes the fracture will be less, see figsures 5.24 and 5.25, thus increasing the probability of having a single atomically sharp microtip on the end of the wire. There is the added difficulty with this technique of the continuing etching of the tip once the separation has taken place, but this can be overcome

Figure 5.23: *Jagged tip produced as a result of fracture of wire as a result of lacquer coated tips.*

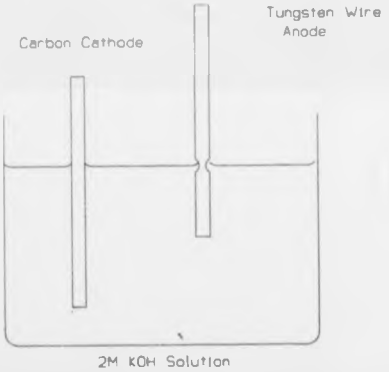

Figure 5.24: *Tip production using the surface miniscus technique.*

Figure 5.25: *Sharper tips produced via miniscus etching method.*

to a certain extent by careful vigilance or by using a power supply that has a cut off if it detects a sudden drop in etching current which will happen when the lower section becomes separated.

In order to improve tip production, a tip etching device was produced that took into account the lessons learned from the above methods. This device holds both ends of the wire in place, therefore leaving no gravitational forces to act on the necking process and allowing it to proceed to complete separation of the wire by etching alone. The piece of wire to be used as the tip is the one that becomes separated from the power supply and for which etching ceases immediately, see figure 5.26. The ability to alter the length of wire exposed to the solution was also incorporated into the device by the use of two simple PTFE slide rods. This gave the facility of selecting the general tip profile. Tips produced using this technique proved to have radii of the order of a few tens of nanometers when examined in a scanning electron microscope.

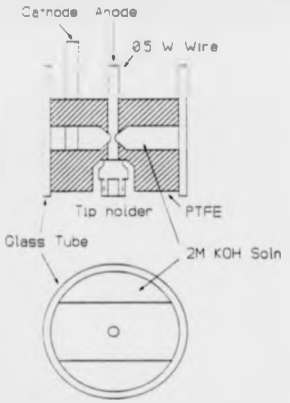

Figure 5.26: *PTFE tip holder, the tip becomes detached from the power supply immediately after it is formed.*

Once these tips had been placed in vacuum they were further prepared by applying a large tunneling current, 10's of nanoamps, for a two to three minute period, which seemed to improve the tips ability to produce atomic resolution images. A similar procedure could revitalise damaged tips. When the imaging ability of a tip appeared to deteriorate, a voltage pulse of between 100 and 200 volts was applied for a fraction of a second. This method is thought to remove any contaminant species that may have become attached to the end of the tip, although the polarity of the pulse was not always the same and the result not always consistent.

5.8 Electrical connections and computer software.

All electrical wiring was effected using shielded silver stranded core coaxial cable with PTFE insulation, and the cable was clamped firmly to the microscope in three places, to the supporting bracket, to the cradle and, to an intermediate damping plate. The connection to the tip passed vertically down the centre of the piezo tube, whose inner electrodes were earthed to help prevent noise in the tunneling current, see figure 5.27. The sample connection was made via a leaf spring that engaged when the sample holder was inserted in the STM. High voltage BNC feedthroughs were used for all connections to the vacuum chamber.

The computer software for the control of the H.T. piezoelectric power supply and for the image display equipment was supplied by W.A. Technology of Cambridge.

5.9 Drift.

A significant problem is caused by mechanical drift in the STM. This term is a general one and refers to the lateral movement of the tip relative to the sample surface over a period of time. A number of factors are involved in causing drift.

1. Thermal drift of the instrument due to the different coefficients of expansion of the materials used in the construction of the instrument. This can be reduced by the careful selection of the constituent materials and the close control of the STM thermal environment.

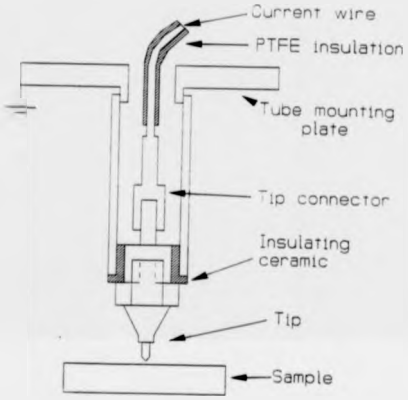

Figure 5.27: *Electrical connections to the tip.*

2. Piezoelectric creep of the tip due to the long time period for the relaxation of the material. By careful selection of the piezoelectric material this can be kept to a minimum.

3. Mechanical relaxation resulting from stresses, either inherent in the material or induced by design. This feature is most often seen in the springs and levers used in the approach mechanisms.

The rate of drift of this instrument was kept to a minimum by the careful material selection and design for each component.

5.10 Overall design schematic.

An overall schematic diagram showing the relative positioning of each of the constituent elements discussed in this chapter is shown in figure 5.28.

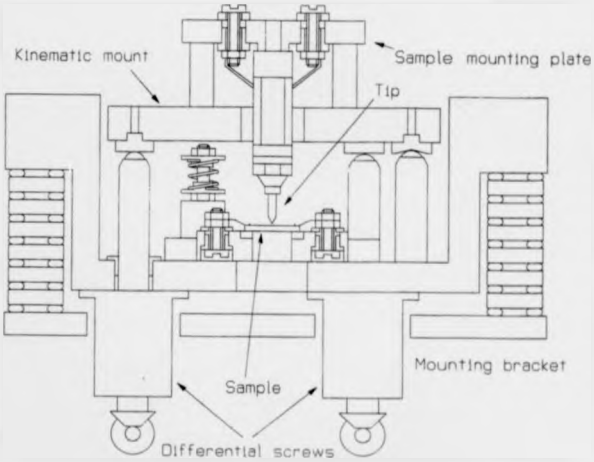

Figure 5.28: *Overall schematic and photograph of STM vacuum head.*

References

[1] Barry Controls, vibration, shock, noise catalogue.

[2] R G Carr, J of Microscopy 152 No.2 (1988) p379

[3] A J Melmed, J Vac Sci Technol B9 (1991) p601

[4] M Okano et al, J Vac Sci Technol A5 (1988) p3313

[5] S -I Park and C F Quate, Rev Sci Instrum 58 (1987) p2004

[6] D W Pohl, IBM J Res Dev 30 (1986) p417

[7] S T Smith, D G Chetwynd and D K Bowen, J Phys E: Sci Instrum 20 (1987) p977

Chapter 6

Preliminary Results and Calibration.

Contents

6.1 Introduction.

Before placing the STM in the UHV chamber a series of tests were carried out under atmospheric conditions. These allowed a number of elementary problems to be eliminated more easily without the delays associated with obtaining the necessary vacuum. By allowing the STM to be operated away from the vacuum chamber on an independent vibration damping system any source of vibrations could also be identified and eliminated, or reduced, more easily.

The operation of an STM in air is severely hampered by the need to use both tips and samples that remain free from surface contamination for a period sufficiently long to allow sample mounting and image acquisition, which restricts the number of materials that can be investigated.

The following objectives were set out for the calibration of the instrument.

1. To produce an image in air on an independent vibration system.

2. To produce an image in air on the vacuum system.

3. To produce an image under vacuum.

4. To resolve single atomic steps.

5. To resolve features on atomically flat planes.

Each of these required different sample characteristics. In order that each of the goals could be achieved a number of samples had to be selected. For each of the tasks numbered above the following were used.

1. Sputtered gold on a mica substrate.

2. Sputtered gold on a silicon substrate.

3. As for 2.

4. Rolled gold foil and hydrogen terminated silicon wafers.

5. Highly ordered pyrolitic graphite (HOPG).

The images presented in this chapter were acquired prior to, or as part of, the calibration process. It should therefore be noted that the dimensions of features observed are not necessarily correct.

6.1.1 Tip production for operation in air.

The most commonly used tip material for air imaging is high purity gold produced simply by cutting 0.5mm wire with a razor blade on a glass anvil. In addition to the gold tips an alloy of 90:10 platinum:iridium wire, prepared in a similar way, was used. In the case of the HOPG sample, an electrochemically etched tungsten tip was used. The tips were sufficiently sharp to allow adequate image resolution

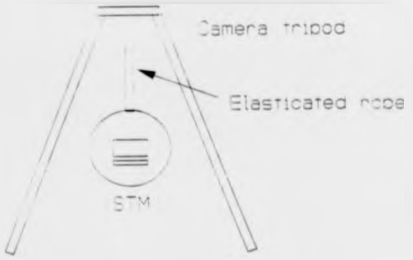

Figure 6.1: *Antivibration mechanism for in air operation of STM.*

of the features to be investigated at each stage.

6.1.2 Vibration isolation.

During atmospheric operation the STM head was suspended from a camera tripod by an elasticated rope (bungee) in a quiet room. After placing the sample in the STM the whole system was steadied manually and then allowed to settle for five to ten minutes, see figure 6.1.

6.2 Gold on mica.

6.2.1 Sample preparation.

Small pieces of Mica approximately 10mm square were cut from Mica sheets to be used as the substrate, clean surfaces for deposition were obtained by cleaving away the upper layers with Cellotape. A number of substrates were then placed in an

Emscope Gold Sputter Coater and a layer of gold several hundreds of Angstroms thick deposited onto the surface over a period of three to four minutes.

6.2.2 Gold on mica.

This first image was obtained using a gold tip and shows gold features of approximately 100Å lateral dimension by 20Å high, see figure 6.2. These values are at the lower end of the range of sizes observed for gold on mica and so the scaling could be assumed to be roughly correct (ie. within a factor of 10). However as the size of features is dependent on the deposition characteristics, a sample prepared in this manner is not an adequate one for a true instrument calibration.

The image itself reveals a noise level which is relatively large when compared to the dimensions of the gold features; on this scale the noise in vertical tip movement is approximately 5 to 10Å peak to peak. An interesting point to note is that even with noise levels of these relatively large dimensions the smaller gold features are still easily distinguishable to the eye.

The distorted curvature of the lower portion of the image is due to hysteresis of the scanning tubes and is only present in the first few scan lines of an image taken shortly after a large lateral tip displacement. If a second image is taken of the same region the distortion is no longer present.

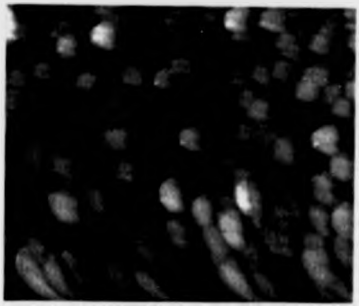

Figure 6.2: *Image of gold on mica taken in air. Line profile is from bottom left to top right of image. Peak to peak line height is nominally 45 Å.*

6.2.3 Gold on mica:- Effect of piezoelectric tube constants.

The computer program controlling the STM has the inbuilt facility to allow the operator to alter the constants governing the voltage applied to the piezoelectric tube per Ångstrom of movement required. This allows the piezoelectric material used to be changed without having to alter the computer programming.

The image in Figure 6.3 was also obtained using a gold tip but the piezo tube constants have been increased from 5Å per volt to 20Å per volt resulting in a multiplication of dimensions by a factor of four. This places the approximate feature size nearer the centre of the range expected, i.e. a few hundred Å laterally by 50 to 70Å high. The noise present on the image has increased by a factor of four giving a peak to peak noise of approximately 30 Å.

The image obtained shows apparently randomly stacked gold clusters, there are smaller clusters under the larger ones giving a granular appearance to the surface.

6.2.4 Surface degradation with exposure to air.

The sample and tip were left in situ for a period of two weeks in air over the vacation. After this prolonged period the surface had changed dramatically, see Figure 6.4, and it is believed that this can be attributed to the mobility of the gold atoms at the surface. The general appearance of the surface is similar to that obtained by Putnam et al [1] when depositing gold on mica at raised substrate temperatures. This would suggest that mobility is the cause of the transformation

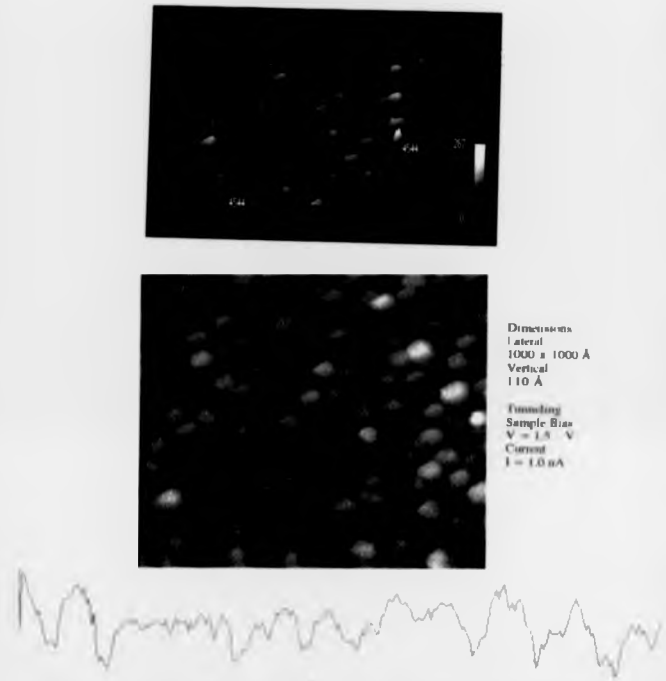

Figure 6.3: *Image of gold on mica taken in air. Line profile is from bottom left to top right of image. Peak to peak line height is nominally 145Å.*

but that it takes longer to occur at room temperature.

The gold layer applied to the mica was very thin and easily damaged. Problems occurred when fixing the sample using the spring clips which scratched off the gold and, because mica does not conduct, lost the connection for the tunnel current. The same problem also occurred during scanning when a tip crash occurred. The tip pierced the gold layer and then continued to extend deep into the mica in an attempt to find a tunnel current, damaging the sample and tip. An alternative conducting substrate was needed. It was decided to use silicon because even if the gold film was removed near the clips a tunneling current would still flow when a voltage above the band gap was applied as the sample bias.

6.3 Gold on silicon.

6.3.1 Sample preparation.

The silicon substrates were cut from wafers orientated in the (100) plane by scratching the surface and applying pressure to crack the wafer over a raised edge. These were then cleaned in ethanol in an ultrasonic bath before having the native oxide removed in an HF:ethanol dip, the procedure for this is described later. A layer of gold a few hundred Ångstroms thick was then applied to the surface using the gold sputter coater.

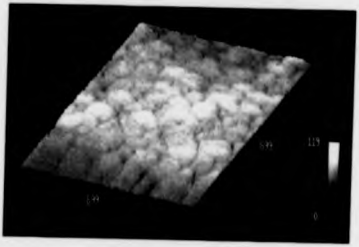

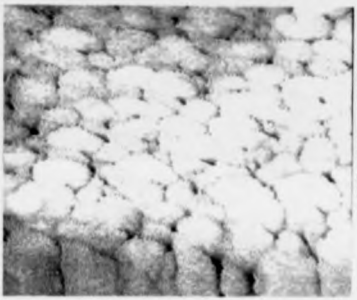

Figure 6.4: *Images of gold on mica taken after two weeks in air. Line profile is from bottom left to top right of image. Peak to peak line height is nominally 50Å.*

6.3.2 Gold on silicon in air.

The image in figure 6.5 was taken in air using a gold tip, the general appearance of the surface is very similar to that of gold on mica and has features of similar dimensions, with the semiconducting nature of the silicon substrate preventing tip crashes on areas void of gold the silicon proved to be a good substitute for the mica. The noise levels on the image are shown in the line profile and are very similar to those observed on the mica substrates. Having established that the sample and tip performed reasonably well in air it was then moved into the vacuum chamber and an image taken under the vibrational conditions that would arise during vacuum experimentation. The image in figure 6.6. was produced in the vacuum chamber but whilst the chamber was at atmospheric pressure. The noise levels are not significantly different to those experienced away from the chamber and it became apparent that the noise due to vibration would need to be reduced on the vacuum rig if atomic resolution was to be achieved.

6.3.3 Gold on silicon under vacuum.

This is the first image to be taken under vacuum and with a tungsten tip, see figure 6.7. The noise levels again are not significantly different to those for previous images and the features are very much the same. In this case however the Tungsten tip used would have been contaminated within a very short time of being produced. The change in resolution across the central region of the image is thought to be due to the rearrangement of the adsorbed contaminants on the tip during the scan. A sudden alteration of resolution in STM work is very common

Figure 6.5: *Images of gold on silicon taken in air. Line profile is from bottom left to top right of image. Peak to peak line height is nominally 500Å.*

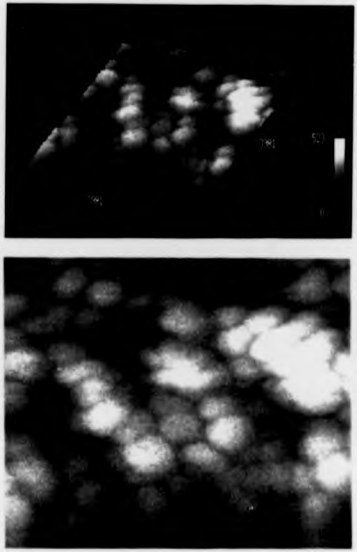

Figure 6.6: *Images of gold on silicon taken in air, but bolted to the vacuum chamber. Line profile is from bottom left to top right of image. Peak to peak line height is nominally 250Å.*

and is mainly attributed to an alteration in the physical, and thus electronic, structure of the tip.

In order to improve tip performance a number of voltage pulses were applied to it, this has the effect of reordering the tip geometry and thus may improve image resolution.

6.4 Rolled gold foil.

6.4.1 Introduction.

The goal now was to obtain resolution of single step edges in air. For this, gold foil was chosen rather than the sputtered material. If the foil is rolled and annealed it forms crystalline (111) faces as well as some more amorphous structures. These crystal faces are quite small and difficult to locate with the eye. As a result the sample had to be moved a number of times before an uncontaminated, well orientated crystal surface was located.

6.4.2 Sample preparation.

The rolled gold had been annealed previously and so only cleaning of the sample was required. This was carried out by placing the samples in an ultrasonic bath of propanol for up to one hour. These were then dried with a hot air blower and placed on the sample stub.

Figure 6.7: *Images of gold on silicon taken under vacuum. The change in noise level across the centre of the image is probably due to the tip reordering. Line profile is from bottom left to top right of image. Peak to peak line height is nominally 470Å.*

6.4.3 Rolled gold foil in air.

Figure 6.8 shows the general features observed on the sample when scanning a non-crystalline area. The great improvement in noise due to the alterations made to the STM can be clearly seen.

6.4.4 Rolled gold foil in air showing single atomic step resolution.

This image shows a series of step edges separated by large flat planes, see figure 6.9. There are no features visible on the lower plane but on the upper plane in the top right of the image a gentle undulation is visible. This is due to the large scale reordering of the (111) surface. True step heights on Au(111) are 2.3Å; the plane to the lower left of the image shows no structure, other than that produced by the levelling computation routines.

6.5 Highly ordered pyrolitic graphite (HOPG).

6.5.1 Difficulties in HOPG imaging.

A great number of groups have imaged HOPG in an attempt to calibrate their STMs. This is indeed an excellent choice because the surface remains clean in air for a period long enough for imaging to take place. The ease of sample preparation allows a number of samples to be prepared and examined with little effort. Single atomic step heights are well known for graphite but during scanning the edges of these steps appear to lift due to tip-sample interactions. The observations of

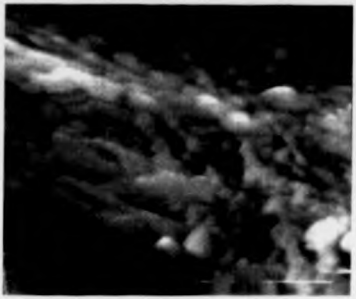

Dimensions
Lateral
2000 x 2000 Å
Vertical
150 Å

Tunneling
Sample Bias
V = 1.5 V
Current
I = 1.0 nA

Figure 6.8: *Images of rolled gold taken in air. Showing some of the large areas of non structured surface. Line profile is from bottom left to top right of image. Peak to peak line height is nominally 100Å.*

Figure 6.9: *Images of rolled gold taken in air. Line profile is from bottom left to top right of image. Peak to peak line height is nominally 45Å.*

periodic features on the atomic planes of graphite do allow it to be used as a calibration for lateral resolution. Unfortunately the very large Z scale of these features shows them not to be true atomic features and as a result we are unable to use graphite as an accurate method for determining the true Z calibration of the instrument. The atomic configuration of the planes of graphite is given in Figure 6.10.

The atoms on each ring are not identical, three atoms marked A have atoms positioned directly beneath them one layers below whereas the atoms marked B do not. This results in a difference in electronic structure [2], that only allows the periodicity characterised by the atom marked B to be imaged. The result is an image of a hexagonal structure, but as this is made up of only alternate atoms there is an feature located in the centre of the hexagon. The rows of features that become apparent are spaced at intervals of 2.1Å and are placed on a hexagonal mesh. The actual Z dimensions obtained while imaging graphite are not so easily explained as they are believed to be a result of both tunneling from tip to sample and the lateral slipping of graphite planes as a result of forces applied by the tip. Graphite is therefore a good material to use for the calibration of the X and Y pieces but it is not suitable for the calibration af Z.

6.5.2 Sample and tip preparation.

Small pieces of HOPG about 10mm square were cut from an old graphite X-ray monochrometer crystal. A clean surface was produced by removing the upper layers of graphite with a piece of Cellotape and the sample was subsequently

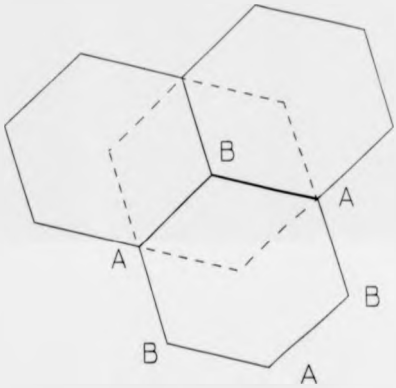

Figure 6.10: *The two atomic sites of HOPG, A with next layer atom immediately beneath and B with no immediate neighbour below.*

mounted on the sample holder before being placing in the STM. A number of samples were prepared in this way as it proved difficult to produce a surface that did not flake. Two different tip materials were used to image the HOPG. These were gold tips produced as for the gold on mica images and tungsten (which does not remain clean in air) sharpened on a grinding wheel.

6.5.3 HOPG in air, single atomic steps.

The image in Figure 6.11 is of HOPG was taken in air under the same conditions as for the gold on mica images. The gold tip used made single atomic steps clearly visible and also shows atomically flat planes. It should be noted that the surface, although relatively smooth, does not show any ordered features at atomic resolution, the features visible on the planes being due to artifacts of the scanning, plane subtraction and levelling computational routines. The steps are approximately 3.35 Å high and show unexpected uneven edges. The reasons for this are not known.

6.5.4 HOPG in air, lateral atomic resolution.

Figure 6.12 is an image of an atomic plane of graphite was obtained using a hand ground tungsten tip. The resolution of the image however is sufficient to show clearly the periodicity expected from the surface. It is unlikely that the tip remained in the vacuum tunneling regime above the surface as it is not thought possible to produce an atomically sharp tip in this way or for the tungsten to remain free from contamination. The image is thought to have been produced by

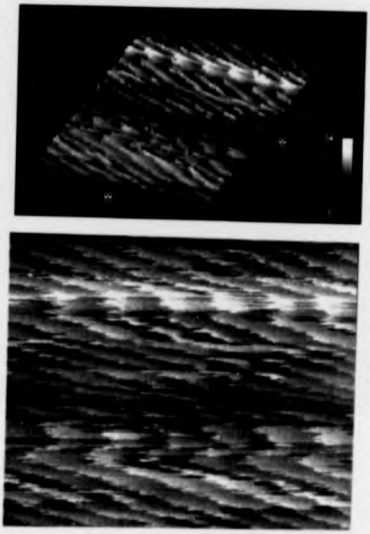

Figure 6.11: *Image of HOPG taken in air. The single atomic steps are clearly visible.*

the tip becoming attached to a layer af graphite and drawing it over the lower graphite layers. The true periodicity of the rows is 2.1Å. This image was used to calibrate the X and Y piezoelectric constants of the STM.

6.6 Silicon

Silicon has become one of the standard imaging materials for the determination of atomic resolution in an STM. The majority of images were taken under UHV conditions in order that the surfaces remained free from contamination, it is however possible to take images if the surface is terminated with an adsorbate to prevent further reaction with the atmosphere. The images presented in this section were taken in air, after terminating the silicon dangling bonds with hydrogen.

6.6.1 Sample and tip preparation.

The silicon samples were supplied by Dr Alan Pidduck of the RSRE Malvern. The (100) p-type samples were boron doped to approximately $2\times10^{17}cm^{-3}$ with a resistivity of approximately 0.1Ωcm. The silicon (111) n-type samples were phosphorus doped to approximately 3×10^{14} to $4\times10^{15}cm^{-3}$ with a resistivity of approximately 1 to 10Ωcm. The native oxides were removed by etching with hydrofluoric acid, which is a technique commonly used in the microelectronics industry. The etch used was a solution of HF and ethanol, the purity of the ethanol being the determinant factor of the final cleanliness of the silicon surface.

The procedure used for etching the samples was the same as that used by Thornton [3] This involved an etch of 2 minutes duration in a solution of 5%

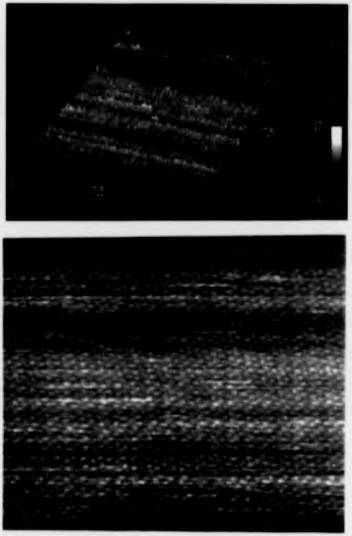

Figure 6.12: *Atomic resolution image of HOPG (approx. 70 Å square). The rows of atoms are 2.1Åapart, z-section is of zoomed region along a row of four atoms.*

HF:ethanol. The contamination left on the surface by oxide, carbon and fluorine has been found to be less than a few per cent of a monolayer and to remain at this level for a number of hours. The samples were cleaved to a size of 10mm square prior to etching and mounted on the sample stub in the usual way.

The tips used were of gold or platinum:iridium for the images taken in air. The UHV images were taken with a tungsten tip.

6.6.2 Imaging HF etched silicon(111).

The first image, figure 6.13, is of HF etched Si(111) taken under atmospheric conditions. The steps are clearly visible but no clear structure is visible on the terraces. The sample was then placed in the vacuum chamber and annealed in an attempt to produce a Si(111)(7×7) reconstruction. Unfortunately the sample heater was unable to heat the sample to the necessary temperature to form the reconstruction, having been designed for use with metal samples. Figure 6.14 is an attempt to image the reconstruction, although there is some structure on the terraces it does not have the true (7×7) reconstruction. A partial formation of the (7×7) structure was observed by Binnig and Rohrer in their early work, but no images were published.

6.7 Discussion.

This chapter has given an insight into STM calibration, both in air and UHV. The instrument has single atomic step resolution on semiconductor and metal surfaces with piezo constants for X and Y of 140Å/V and Z of 40Å/V.

Figure 6.13: *HF etched silicon (111) imaged in air.*

Figure 6.14: *HF etched silicon (111) annealed and imaged under UHV.*

References

[1] A Putnam, B L Blackford, M H Jericho and M O Watanabe, Surf Sci 217 (1989) p276

[2] D Tománek, S G Louie, H J Mamin, D W Abraham, R E Thomson, E Ganz and J Clarke, Phys Rev B35 (1987) p7790

[3] J M C Thornton, PhD Thesis, Univ Wales College Cardiff (1990)

Chapter 7

The Reconstruction of Oxygen Induced Facets on Vicinal Copper Surfaces.

Contents

7.1 Introduction.

It is well known that oxygen adsorption causes copper surfaces to undergo one of two forms of reconstruction. The faceting of vicinal surfaces cause microscopic morphological changes whereas the adsorption of oxygen onto low index faces produces reconstructions at the atomic level. The latter is well documented for both the Cu(110)(2×1)-O and the Cu(100)($2\sqrt{2} \times \sqrt{2}$)-O missing row reconstructions which involve both substrate movements and the ejection (or addition) of rows of copper atoms.

This chapter describes the investigation of faceting of copper surfaces due to oxygen adsorption, using the STM described earlier in this thesis. A review of relevant previously observed oxygen induced reconstructions is given together with a description of previously proposed models. The images obtained with the STM in the present work are discussed and a model for the reconstruction of the facets is proposed.

7.2 Theoretical background.

A theory that effectively describes metal-adsorbate systems is the Effective Medium Theory (EMT) [27]. This theory assumes that an atom in a metallic environment is effectively screened from the detailed structure surrounding it. In this theory the assumption is made that the total electron density of the system can be described by the superposition of the electron densities of each of the atoms in the system, see equation 7.1.

$$n(r) = \sum_i n_i(|\, r - R_i \,|) \tag{7.1}$$

The atomic-electron density $n_i(r)$ for atom i is the density induced by the atom embedded in a homogeneous electron gas. The density of this gas is dependent on the average of the electron density tails of the surrounding atoms. The assumption thus takes into account the average effect of neighbouring atoms, so including approximations of effects such as screening and charge transfer. If this system is now used together with a similar approach for the one-electron potentials, an expression for the total energy of the system can be obtained, see equation 7.2.

$$E_{tot} = \sum_i E_{c,i}(\overline{n}_i) + E_{AS} + E_{1el} \tag{7.2}$$

Here the cohesive function $E_{c,i}(\overline{n}_i)$ is obtained from the embedding energy of atom i in a homogeneous electron gas of density n_i. The minimum in the cohesive function of an atom displays the tendency of that atom to form chemical bonds of a length that allows the atom to occupy a position in an electron density close to the optimum. See figure 7.1. The cohesive functions for hydrogen, oxygen and sulphur are plotted [27]. The optimum electron density for the adsorption of oxygen can be seen to be greater than the optimum distance for the other two, this implies that the oxygen chemisorption bond length would be expected to be shorter than the other two. This is indeed the case as oxygen is known to adopt sites well embedded in the sample surface. The expression for the atomic-sphere correction (E_{AS}) and the one electron energy difference (E_{1el}) account for the changes in energy when atom i is taken from a homogeneous electron gas to a

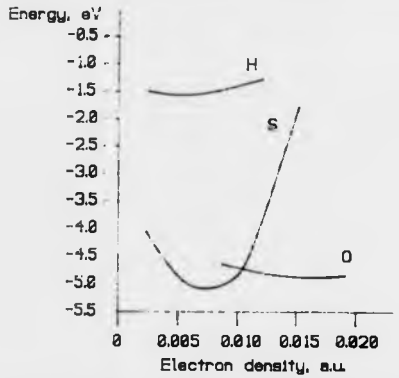

Figure 7.1: *The cohesive function E_c for oxygen, hydrogen and sulphur calculated using the self-interaction correction to the local density approximation. After Bezenbacher and Nørskov [9].*

real system.

$$E_{tot} = \sum_i \left[\int_{-\infty}^{\varepsilon_F^{real}} d\varepsilon \varepsilon \Delta n_i^{real}(\varepsilon) - \int_{-\infty}^{\varepsilon_F} d\varepsilon \varepsilon \Delta \overline{n}_i(\varepsilon) \right] \qquad (7.3)$$

An expression for E_{tot} is given in equation 7.3 where $\Delta n_i^{real}(\varepsilon)$, ε_F^{real}, and $\Delta \overline{n}_i(\varepsilon)$, ε_F are the induced densities of states of atom i and the Fermi energy in the real metal and in the homogeneous electron gas respectively. In a free electron gas type environment the final term can be ignored, but for chemisorbed oxygen, for which the interaction with the metal d band is strong, this term becomes extremely important.

7.3 Review of the chemisorption of oxygen on copper.

This section describes the oxygen induced faceting and reconstruction of copper surfaces that are relevant to the investigation of the faceted Cu(410)-O surface.

7.3.1 Chemisorption of oxygen on vicinal copper surfaces.

It has been well documented that the vicinal surfaces of copper near to the (100) low index face facet to (410) when exposed to oxygen. LEED studies in the early 70's by Perdereau and Rhead [26] compared the alterations in LEED patterns for a number of surface orientations, varying between 10° and 20° from the [100] pole, when exposed to oxygen. The results showed that the greater the step density, the more rapidly the LEED pattern changed; the conclusion drawn was that the oxygen adsorbed preferentially at the step edges forming a Cu(410) surface structure. An X-ray Photoelectron Diffraction (XPD) investigation of the Cu(410) surface by Thompson and Fadley [31] yielded information on the adsorption sites of the oxygen on the copper surface. The technique involved the comparison of experimental results with single-scattering cluster calculations. The conclusion drawn was that oxygen was found to lie predominantly on the [010] step edge at low exposures with oxygen atoms also occupying the fourfold hollow site on the copper terrace at higher exposures (i.e. above 40L), see figure 7.2.

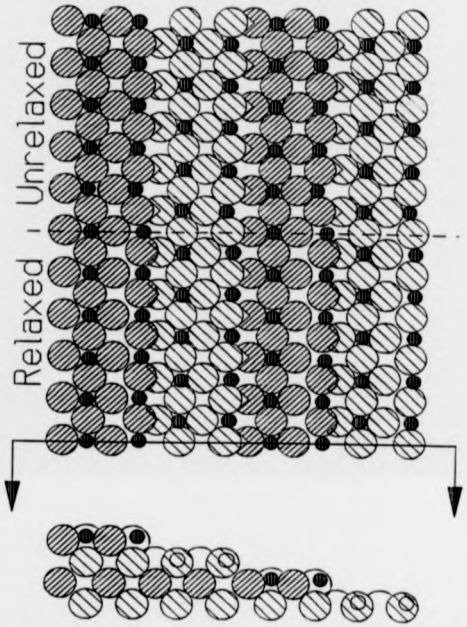

Figure 7.2: *Thompson and Fadley model for the chemisorption of ozygen on Cu(410).*

7.3.2 Chemisorption of oxygen on Cu(110).

The Cu(110) surface is the least densely packed of the low Miller index surfaces with an atomic density of $\sqrt{2}/a^2$ atoms/cm^2 where a, the lattice constant, is 3.615Å, see figure 7.4. At low temperatures the oxygen adsorbs molecularly, but at room temperature it adsorbs dissociatively producing a (2×1) LEED pattern. A coverage of 1/2 a monolayer is achieved after exposure to only a few Langmuir of gas. A number of models have been suggested for the surface reconstruction, these include a buckled row [24, 18], a missing row [32, 9, 20, 7] and an added row [5, 13, 15, 17]. The latter pair are only distinguishable by their growth mechanism and not by their final structure. In all of these studies it was generally agreed that the oxygen is situated in the long bridge site along the [001] direction with a highly directional O-Cu bond along the [001] rows. This conclusion is supported by high resolution electron energy loss spectroscopy (HREELS) [23], inverse photoemission (IPE) [12, 2] and angle resolved ultraviolet photoelectron spectroscopy (ARUPS) [7, 6].

The role of STM in establishing the mechanism of nucleation and growth of these rows has been significant [5, 13, 15, 17]. When a number of STM images are obtained consecutively at increasing exposures it becomes possible to produce dynamic STM videos showing the movement of surface features. These dynamic visualisation STM (DVSTM) images have been obtained for Cu(110) oxygen induced reconstructions [4] and show the migration of Cu atoms from step edges to form -Cu-O-Cu- chains on the terraces. These chains are perpendicular to the close packed [$\bar{1}$10] direction, i.e. along the [001] copper rows. At room tempera-

ture the rows are seen to move readily over the surface, showing that Cu atoms are very mobile at this temperature.

Dynamically, the low coordinated Cu atoms diffusing across a terrace are thought to be linked to the dissociated oxygen atoms, also migrating, to form a Cu-O link. These Cu-O links then become attached to the end of a -Cu-O-Cu-O- chain due to the strong Cu-O interaction along the [001] direction to form chains of up to 200Å in length. The chains themselves become stabilised when butted against each other. The Cu adatoms diffusing from the step edges are inhibited due to the density of Cu-O chains and this eventually restricts the supply of Cu atoms from the step edge. It is at this point that a second mechanism becomes dominant. This second mechanism, although it has a higher activation energy, dominates the generation of Cu-O rows when the source of Cu atoms from the step edge has effectively been terminated. Rectangular troughs 1 atomic layer deep are formed on the Cu(110) terraces, and the Cu atoms released by this are incorporated into the -Cu-O- chains on the terraces. The rate of growth of the reconstructed areas decreases, but the whole of the Cu surface eventually becomes reconstructed. The surface generated at room temperature has a large number of defects, such as steps and domain boundaries, due to the pits formed. If the surface is annealed then an almost perfect Cu(110)(2×1)-O structure is formed; alternatively the Cu(110) surface can be exposed to oxygen at an elevated temperature (approximately 370 K) to obtain this well ordered structure.

The mechanism described above allows the three main models to be evaluated. The buckled row model can be dismissed confidently as it is inconsistent

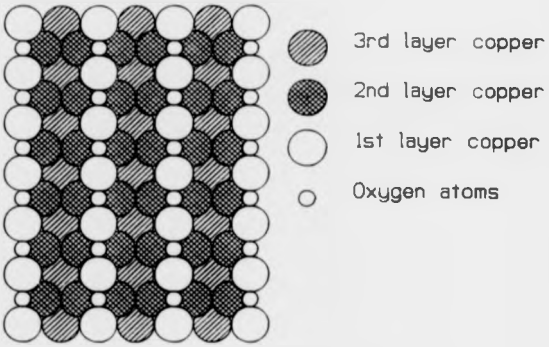

Figure 7.3: *Ball model of Cu(110)(2×1)-O reconstruction.*

with the -Cu-O- chain mobility and the mass transport characteristics of the Cu. The missing row model would suggest a growth of the step edge from vacancies produced in the terrace, this was seen not to be the case, leaving the added row model as the most accurate description of the reconstruction mechanism, see figure 7.3.

At elevated temperatures, above 300K, and at much increased oxygen exposures (approximately 10^6L), a second reconstruction occurs. The Cu(110)(2×1)-O reconstructs to form a c(6×2)-O phase which coexists on the surface with the (2×1)-O reconstruction. The growth of the c(6×2)-O structure nucleates at the step edges and during formation causes the trough dimensions to increase. This is consistent with the model of an increased Cu adatom density on the c(6×2)-O surface, see figure 7.4.

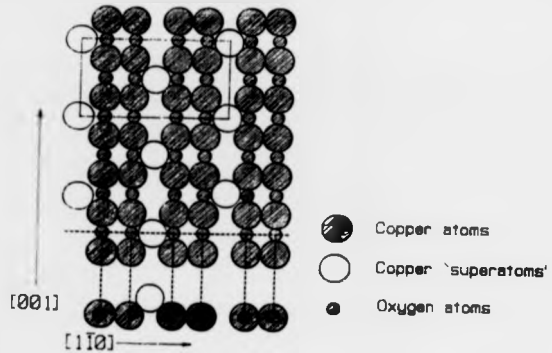

Figure 7.4: *Ball model of Cu(110)c(6×2)-O reconstruction.*

7.3.3 Chemisorption of oxygen on Cu(100).

The Cu(100) surface is a more densely packed surface than the Cu(110) with an atomic density of $2/a^2$ atoms/cm^2. On this surface oxygen adsorbs molecularly at temperatures below 100K, but at room temperature and above it chemisorbs dissociatively.

Two separate structural phases have been reported for the chemisorption of oxygen on Cu(100) at or about room temperature. Firstly some authors report that a $(\sqrt{2} \times \sqrt{2})$R45° or c(2×2) structure was produced, which at higher temperatures or increased oxygen exposure would develop into a $(2\sqrt{2} \times \sqrt{2})$R45° structure. Attempts to determine the oxygen adsorption site in the c(2×2) phase by differing analytical techniques have, however, led to conflicting results. A number of reports have suggested the two fold bridge site [28, 30, 25] and some a

fourfold hollow site, either with the O positioned 1Å above the surface [33, 8, 11], or coplanar with it [25, 16]. Above 300K it has generally been concluded that the c(2×2) structure does not occur, although some ambiguity does exist. Between 220 and 300K conclusive proof has yet to be offered for the exhistance of the c(2×2) phase.

The presence of the $(2\sqrt{2}\times\sqrt{2})$R45° phase, by contrast, is now well established for exposure at temperatures above 300K by the same experimental evidence which eliminated the possibility of the c(2×2) structure. The techniques involved were LEED [22], HREELS [35, 36], STM [14, 34],PhD [1] and XRD [29]. Each of these also confirmed the structure of the $(2\sqrt{2} \times \sqrt{2})$R45° to be a missing row type reconstruction with an oxygen coverage of 1/2 monolayer.

The mechanism for the production of this missing row reconstruction has been observed with DVSTM [14]. A series of consecutive images of the Cu(100) surface were taken at increasing oxygen exposures. The location of the step edge essentially remained fixed as copper atoms began to appear on the previously flat terraces. The atoms formed islands with edges predominantly along the [010] and the [001] directions to cover a total area of 25% of the surface at the saturation oxygen coverage of 1/2 monolayer. This is consistent with the ejection of every fourth copper atom row from the terraces to form a missing row structure. A number of atomic resolution STM images of this structure have been published [14, 13] each showing an ordered pairing of bright spots along the [010] direction with a periodicity of 3.6Å. Along the [$\bar{1}$11] direction perpendicular to the [010] direction the periodicity at which the $(2\sqrt{2} \times \sqrt{2})$R45° structure repeats itself

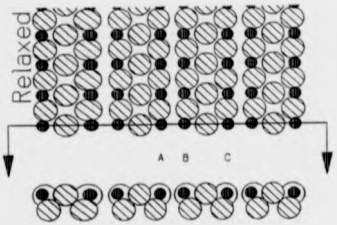

Figure 7.5: *Ball model of a Cu(100)($2\sqrt{2} \times \sqrt{2}$)R45°-O reconstruction.*

is 7.2Å with row separations of 2.9Å and 4.3Å from A to B and from B to C respectively, see figure 7.5.

The images are consistent with the model of -Cu-O- chains along the Cu [001] direction with every fourth Cu [001] row missing. The Cu rows along side the missing row relax into the vacancy with a lateral displacement of 0.3Å [38, 29]. A vertical displacement away from the surface is also suggested for these rows and this is supported by the STM images. The precise extent of the vertical displacement is not yet established but a number of values have been published. Dynamical LEED analysis [38] suggests a displacement of 0.1Å for Δd_0 as well as for Δd_{12} and Δd_{23}, see figure 7.6. These values are in best agreement with the STM images. SEXAFS results [8] yield a Cu-O bond length of 1.94Å, a value close to the average found for the STM images of 1.91Å. It should be noted

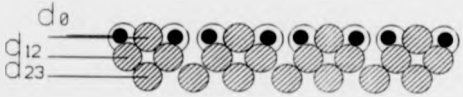

Figure 7.6: *Diagram of dimensions discussed in text.*

that these Cu-O rows can be thought of as stable Cu(110) microfacets and reveal the great similarity between the (2×1)-O reconstructions of the Cu(110) and the $(2\sqrt{2} \times \sqrt{2})R45°$-O reconstruction of Cu(100).

At higher exposures and elevated temperatures a copper oxide grows on the surface. The Cu_2O grows epitaxially on the Cu(100). Studies of the orientation of this oxide growth have been carried out by x-ray diffraction [19, 10].

Conclusion of reviews.

To conclude, on Cu(110) and Cu(100) surfaces it is energetically favourable for the Cu to reconstruct to form -Cu-O- chains along the [001] direction. This is also found to be the case for the terraces of vicinal surfaces close to the (110) and (100) planes.

7.4 Preparation of the Cu(810) crystal surface.

The crystallographic (810) orientation, (this is midway between (100) and (410)), see figure 7.7, was produced by cutting a single crystal copper bar with a spark eroder and mechanically polishing the surface to a 1 micron diamond grit finish. This was then cleaned in acetone in an ultrasonic bath before being dipped in nitric acid for a few seconds to remove some of the damaged copper surface layers. The crystal was then again ultrasonically cleaned in acetone before being washed with propanol prior to placing it in the vacuum chamber. The crystal was then cleaned further by cycles of ion bombardment at 500eV and 7μA for 10 mins and then annealing to 850°C. The cleanliness of the sample surface was determined by AES, see figure 7.8, and the crystallographic orientation and quality of the long range surface order by LEED, see figure 7.9.

7.5 Presentation and interpretation of STM images of oxygen on Cu(810).

The images of copper surfaces presented in this section show an image of the oxide crystallites that are formed when oxygen exposure is of the order of thousands of Langmuirs. The clean Cu(810) surface and the Cu(410) faceted surface induced by oxygen adsorption. Higher resolution images of the Cu(410) facets themselves are then presented that yield information on the possible reconstruction of the (410) terraces themselves.

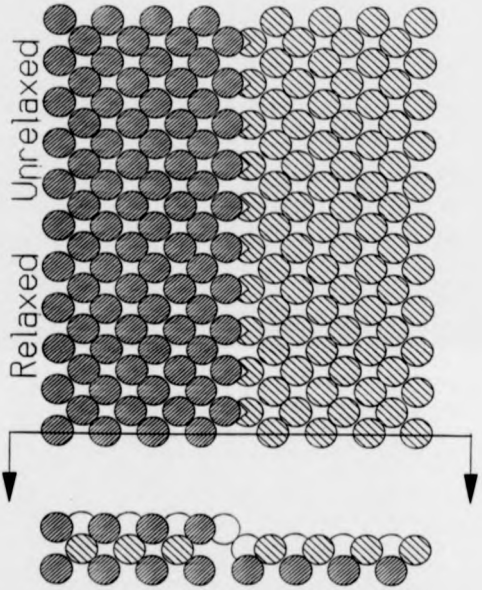

Figure 7.7: *Crystallographic orientation of Cu(810).*

Figure 7.8: *AES spectrum of clean copper surface.*

Figure 7.9: ***LEED pattern of clean Cu(810) surface.***

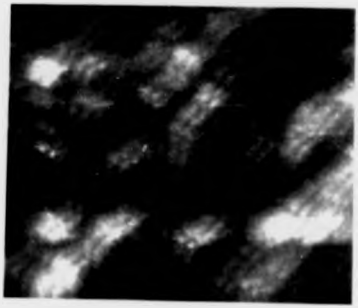

Figure 7.10: *Crystallites formed on the copper surface after exposure to many 1000's of Langmuir of oxygen (approx. 1000Å square).*

7.5.1 The oxygen induced faceting of Cu(810) to Cu(410).

The first image presented is of the crystallites formed by exposures to large amount of oxygen (1000's L), see figure 7.10. The oxide grows with a crystallographic orientation preferentially along the Cu(110) and the Cu(001) direction. The image is 1000 Å square and the corrugations are approximately 30 Å and bear a strong resemblance to those of crystallites on molybdenum [21].

The images presented in figure 7.11 is of 'clean' Cu(810) surface before exposure to oxygen. Figure 7.12 is of the same surface faceted to (410) after exposure to oxygen. The images were obtained using a tunneling current of 1nA with a sample bias of +300mV. The electrons were therefore tunneling from the tip to the sample and the image is of the unoccupied states on the surface. Scan sizes

Figure 7.11: *Image of 'clean' Cu(810) surface (approx. 80Å square).*

were both 1000Å and the images were flattened to a plane, zoomed and rescaled. For a scan of this size the number of data points per terrace is not sufficient for atomic resolution. The images therefore do not yield any information on the steps at the atomic level. The number of data points is only sufficient to allow the general location of the step to be determined. Also it is not possible to determine whether the images are of exactly the same region of surface, because the time taken to dose the surface is sufficient to allow significant lateral drift of the instrument. However, the overall trend in the alteration of the surface structure, however, can be determined.

The acquisition of images of a clean copper surface with a high step density proved extremely difficult, due to the high mobility of the copper atoms. The time between each line scan was long enough for the step edges to move a distance

Figure 7.12: *Image of Cu(410) oxygen induced facets (approx. 80Å square).*

sufficiently large so as to make the adjacent steps on a high step density surface undistinguishable. In fact it was not possible to image clearly a totally clean crystal and the image in figure 7.11 was obtained after dosing the surface with a tiny amount of oxygen ($\ll$1L). This was sufficient to partially pin the step edges but not to cause a reconstruction of the whole surface. A similar effect was obtained by allowing the sample to remain in the STM for a number of hours and become contaminated by the gases present in the vacuum chamber. The partial pinning of the step edges has allowed the mobility of the step edges to be reduced sufficiently for a recognisable image to be acquired.

The terraces on the (810) surface have an average width of approximately 14.5Å separated by monatomic steps. On the (410) faceted surface the average terrace width is reduced by a factor of 2 to 7.2Å, again terminated by a monatomic

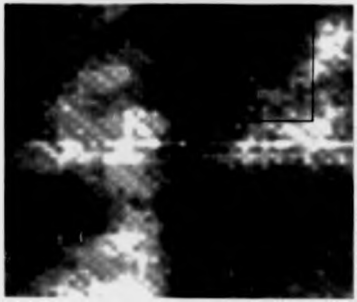

Figure 7.13: *High resolution image of the Cu(410) oxygen induced reconstructionb (approx. 110Å square).*

step. Peak to peak heights over the whole of figures 7.11 and 7.12 are 22Å and 14Å respectively.

7.5.2 High resolution images of the Cu(410) facets.

The image shown in figure 7.13 is of the Cu(410) oxygen induced reconstruction. The size of the scanned area is much less, 110Å square, and therefore atomic resolution of the step edges and terraces is possible. A zoomed region, 43Å square, of the image in figure 7.13 is shown in figure 7.14.

The image displays paired rows of bright spots along the [001] direction with a spacing of 3.6Å. The separation along the [010] direction from step edge to step edge is 7.2Å with internal distances of 3.1Å from rows A to B and 4.1Å from

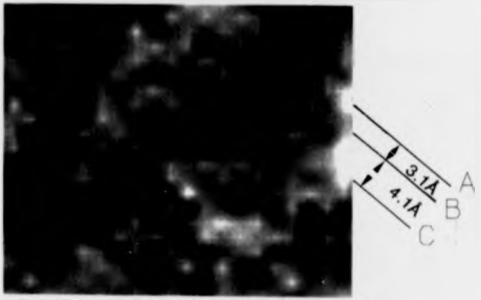

Figure 7.14: *Zoomed image of a section of figure 7.13 (approx. 43Å square).*

rows B to C. The step edges are clearly distinguishable in cross section, see figure 7.15. It should be noted that each pair of parallel rows is displaced along the row direction by half a lattice spacing, 1.8Å, from the last as is consistent with crossing a monatomic step on the Cu(410) surface. See figure 7.2.

7.6 Analysis of results.

In analysing STM images the identity of the atoms on the sample surface being imaged must first be determined. The true physical relationship between the location of the high points of the surface corrugation and the atomic positions is as yet unclear, but as will be shown, in the present case the question as to whether the bright spots reveal the locations of the oxygen or the copper

Figure 7.15: *Cross section of figure 7.14 showing monatomic steps.*

atoms is unimportant. We have established that the electrons are tunneling into the unoccupied states on the sample surface but, as yet, not which of the elements present produces the bright features associated with the points of high tunnel current. One possibility is to assume that in these images the bright spots correspond to the oxygen atoms, a reasonable assumption as the chemisorbed oxygen is believed to have a high density of unoccupied (2p antibonding) states near to the Fermi level, Alternatively we could assume that the bright spots are produced by tunneling into copper atoms at the step and missing row edges, as suggested by recent literature [13]. The main structural conclusions discussed here are found to be insensitive to which of these interpretations we chose.

Superficially the images obtained are in good agreement with the work of both x-ray photoemission diffraction of Thompson and Fadley [31] and the LEED

analysis of Perdereau and Rhead [26]. The Cu(810) surface has faceted to form terrace widths half of the original cut dimensions i.e. a Cu(410) surface. The rows of bright spots along the [001] direction would be consistent with the positioning of the oxygen atoms along the [001] step edges and an adjacent fourfold hollow site on the terrace. (An alternative interpretation is to correlate the bright spots with copper atoms midway between oxygen atoms along the [001] direction in this model.)

On closer inspection however, the spacing of the features along the direction perpendicular to the step edge appears to be inconsistent with this model. If one assumes that the oxygen atoms adsorbed at the step edge relax outwards away from its neighbours on the terrace (as occurs for the oxygen atoms relaxing into the missing row of the analogous Cu(100)($2\sqrt{2} \times \sqrt{2}$) reconstruction, see figure 7.16) then the narrower of the two row spacings would need to be between the pair of oxygens that lie across the step edge and not between the pairs on the terrace, as observed in our STM results. Unfortunately the narrowing of the gap between oxygen rows on the terraces can not be achieved if the oxygen atoms are adsorbed in the simple fourfold hollow site shown previously in figure 7.2, as this position effectively constrains any lateral movement of the oxygen. Similar arguments apply to the copper atoms if these are the imaged species.

A reconstruction of the Cu(410) facets has recently been proposed by Robinson et al [29]. In this case they suggest a missing copper atom row, specifically the [001] row along the base of a step edge, see figure 7.17. This would produce terraces on the Cu(410) surface that were exactly analogous to the Cu(100)

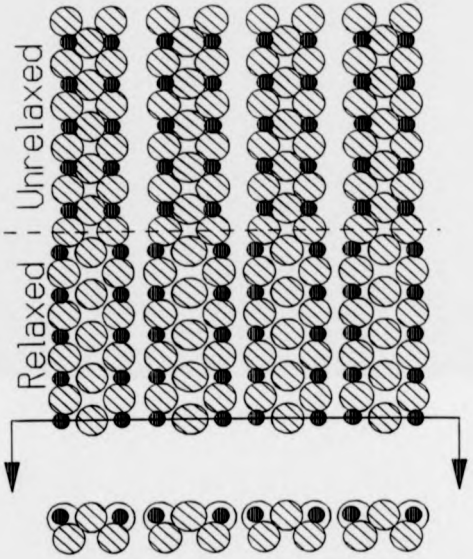

Figure 7.16: *Ball model of Cu(100)(2$\sqrt{2}$ × $\sqrt{2}$)-O reconstruction.*

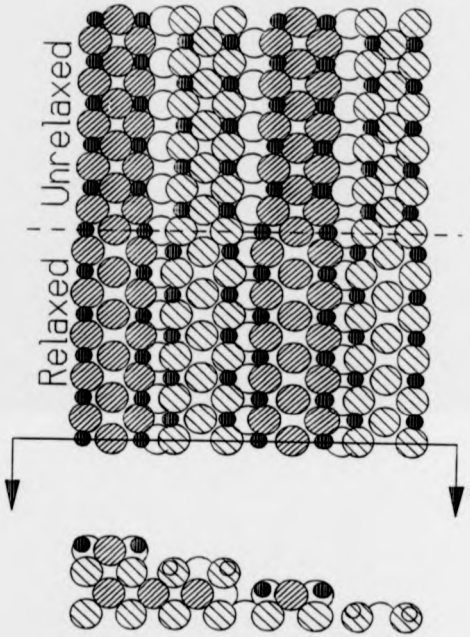

Figure 7.17: *Ball model of Robinson missing row reconstruction of Cu(410).*

oxygen reconstructed surface. The benefits energetically in forming this surface reconstruction are not clear, as the ejection of the row and the subsequent increase in surface area would need to be compensated for. The relaxation arround the missing row in this model would require a narrowing of the spacings in the STM image between the oxygen or copper atoms across the step edges, again inconsistent with our observations.

In order to interpret our results a model must be created that allows for a narrowing of the spacing between the oxygen or copper rows on the same terrace, combined with an increase in the inter-row spacing across the step edge. This can only be achieved if the oxygen atoms and their neighbouring copper atoms positioned centrally on the terraces are allowed to relax towards the row of atoms located at the step edge of the same terrace. The possibility of an alternative missing row reconstruction of the Cu(410) terrace must now arise. If the [001] copper row positioned one atom in from the step edge is removed, the previously constrained oxygen and copper atoms within the terrace become step edge atoms as in the Cu(100)$(2\sqrt{2}\times\sqrt{2})$R45° missing row model, see figure 7.16. This would allow the oxygen and copper atoms to relax laterally outwards away from the terrace and towards the vacated row. This would also result in an alteration of the environment of the original Cu(410) step edge atoms. These no longer sit at the edge of a terrace, but occupy the highly prefered Cu-O-Cu chain identical to that of the Cu(110)(2×1)-O reconstruction, see figure 7.18.

On closer inspection this model offers a much preferred step edge type adsorption site for all oxygen atoms, allowing them to occupy almost coplanar sites

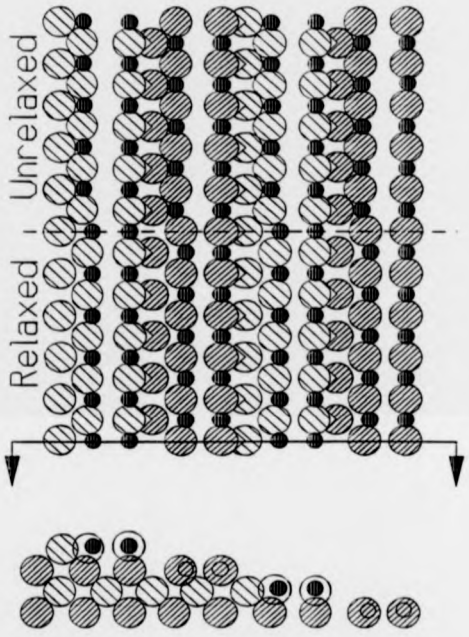

Figure 7.18: *Proposed model for the ozygen reconstruction of Cu(410).*

on the copper surface. The simple fourfold hollow overlayer terrace site, which is presumed to be unstable due to the large charge transfer that is predicted to occur, need no longer be considered. The almost coplanar adsorption site that arises also satisfies the close coordination desired by oxygen seeking a high surrounding electron density as discussed in the effective medium theory section of this chapter.

7.7 Conclusions.

Previously published work on oxygen adsorption on Cu(100 and Cu(110) have shown the strong tendency of oxygen to adsorb on copper in linear Cu-O-Cu chains that allow the oxygen to lie almost coplanar with the copper surface.

The images presented in this chapter have resulted in the creation of a model for the reconstruction of oxygen induced Cu(410) facets that allows both oxygen adsorption sites to be of this Cu-O-Cu chain type. The formerly considered terrace edge site becomes a Cu(110)(2×1)-O chain structure where as the previously mid-terrace, now missing row edge oxygen atom, occupies a position very similar to that of the Cu(100)($2\sqrt{2} \times \sqrt{2}$)R45°-O chain structure producing a surface that is believed to be energetically more favourable

References

[1] M C Asensio, M J Ashwin, A L D Kilcoyne, D P Woodruff, A W Robinson, Th Linder, J S Somers D E Ricken and A M Bradshaw, Surf Sci 236 (1990) p1

[2] E Bertel, Appl Phys A 53 (1991) p356

[3] F Besenbacher and J K Norskov, Oxygen chemisorption on metal surfaces: general trends for Cu, Ni and Ag. (1992)

[4] F Besenbacher, F Jensen, E Lægsgaard, K Mortensen and I Stensgaard, Jour Vac Sci Tech B 9 (1991) p874

[5] D J Coulman, J Wintterlin, R J Behm and G Ertl, Phys Rev Lett 64 (1990) p1761

[6] R Courths, B Cord, H Wern, H Saalfeld and S Hüfner, Solid State Comm 63 (1987) p619

[7] R A DiDio, D M Zehner and E W Plummer, J Vac Sci Tech A 2 (1984) p852

[8] U Döbler, K Baberschke, J Stöhr and D A Outka, Phys Rev B 31 (1985) p2532

[9] R Feidenhans'l and I Stensgaard, Surf Sci 133 (1983) p453

[10] F Grønlund and P E Højlund Nielsen, Surf Sci 30 (1972) p388

[11] S P Holland, B J Garrison and N Winograd, Phys Rev Lett 43 (1979) p220

[12] W Jacob, V Dose and A Goldmann, Appl Phys A 41 (1986) p145

[13] F Jensen, F Besenbacher, E Lægsgaard and I Stensgaard, Phys Rev B 41 (1990) p10233

[14] F Jensen, F Besenbacher, E Lægsgaard and I Stensgaard, Phys Rev B 42 (1990) p9206

[15] F Jensen, F Besenbacher, E Lægsgaard and I Stensgaard,in The Structure of Surfaces III, eds S Y Tong, M A Van Hove, K Takayanagi and X D Xie, vol 24, Springer Verlag Berlin (1991) p462

[16] S Kono, S M Goldberg, N F T Hall and C S Fadley, Phys Rev Lett 43 (1978) p1831

[17] Y Kuk, F M Chua, P J Silverman and J A Meyer, Phys Rev B 41 (1990) p12393

[18] J Lapujoulade, Y Le Cruër, M Lefort, Y Lejay and E Maurel, Surf Sci 118 (1982) p103

[19] K R Lawless and A T Gwathmey, Acta Metallurgica 4 (1956) p153

[20] K S Liang, P H Fuoss, G J Huges and P Eisenberger in The structure of surfaces, ed M A van Hove and S Y Tong, Springer series in surface science, vol 2, Springer Verlag, Berlin (1985) p246

[21] B Marchon, D F Ogletree, M E Bussell, G A Somorjai, M Salmaron and W Siekhaus, Joural of Microscopy 152 Pt2 (1988) p427

[22] R Mayer, C S Zhang and K G Lynn, Phys Rev B 33 (1986) p8899

[23] J M Mundenar, A P Baddorf, E W Plummer, L G Sneddon, R A DiDio and D M Zehner, Surf Sci 188 (1987) p15

[24] H Niehus and G Comsa, Surf Sci 140 (1984) p18

[25] J H Onuferko and D P Woodruff, Surf Sci 95 (1980) p555

[26] J Perdereau and G E Rhead, Surf Sci 24 (1971) p555

[27] M Puska and R Nieminen, Phys Rev B 43 (1991) p12221

[28] H Richter and U Gerhardt, Phys Rev Lett 51 (1983) p1570

[29] I K Robinson, E Vlieg and S Ferrer, Phys Rev B 42 (1990) p6954

[30] A Scheidt, H Richter and U Gerhardt, Surf Sci 205 (1988) p38

[31] K A Thompson and C S Fadley, Surf Sci 146 (1984) p281

[32] L H Tjeng, M B J Meinders and G A Sawatzky, Surf Sci 233 (1990) p163

[33] J G Tobin, L E Klebanoff, D H Rosenblatt, R F Davis, E Umbach A G Baca, D A Shirley, Y Huang, W M Kang and S Y Tong, Phys Rev B 26 (1982) p7076

[34] Ch Wöll, R J Wilson, S Chiang, H C Zeng and K A R Mitchell, Phys Rev B 42 (1990) p11926

[35] M Wuttig, R Franchy and H Ibach, Surf Sci 224 (1989) pL979

[36] M Wuttig, R Franchy and H Ibach, Surf Sci 213 (1989) p103

[37] H C Zeng, R A Macfarlane and K A R Mitchell, Surf Sci 208 (1989) pL7

[38] H C Zeng and K A R Mitchell, Surf Sci 239 (1990) pL571

Chapter 8

Summary.

Contents

8.1 Summary of the design and development.

The aims of this project were to design, build and operate an STM for use in a UHV chamber capable of resolving adsorbed molecules or atoms on a single crystal metal surface. The procedure followed in order that this goal could be achieved involved the testing of the instrument in air prior to vacuum operation. Many modifications to the instrument were carried out as a result of this test procedure, the details of which have not been presented in this thesis. The instrument described in chapter 5 is the result of these alterations and is described in the configuration in which it was used to produce the results presented in chapter7.

The preliminary results presented in chapter 6 were obtained during the test procedures and show how the resolution of the instrument gradually improved to

a point where atomic resolution was thought to be achievable on metal adsorbate systems. This initially proved not to be the case and some modifications had to made to the wiring of the STM head.

8.2 Summary of results.

The oxygen induced faceting of vicinal copper was chosen as the first system to investigate not only for the scientific interest but also for the relatively large scale of the features, i.e. monatomic steps 1.8Å high spaced 7.2Å apart, compared to low Miller index faces.

The results obtained revealed more than had been originally anticipated, with the observation of double rows on the copper terraces. The analysis of these features in greater detail lead to the development of a new model for the reconstruction of the Cu(410) terraces.

8.3 Future work.

The results presented in this thesis present a new model for the adsorption of oxygen on stepped copper surfaces. The model presented needs further investigation with a true quantitative technique such as LEED. The actual STM head itself could now also be greatly improved by redesigning the system using the knowledge and experience gained over the duration of this project.